LASER SYNTHESIZED GOLD NANOPARTICLES FOR HIGH SENSITIVE STRAIN GAUGES

A THESIS

SUBMITTED TO THE MATERIALS SCIENCE AND

NANOTECHNOLOGY PROGRAM

AND THE GRADUATE SCHOOL OF ENGINEERING AND SCIENCE

OF BILKENT UNIVERSITY

IN PARTIAL FULFILLMENT OF THE REQUIREMENTS

FOR THE DEGREE OF

MASTER OF SCIENCE

By

Salamat Burzhuev

December, 2013

I certify that I have read this thesis and that in my opinion it is fully adequate, in scope and in quality, as a thesis for the degree of Master of Science.

Asst. Prof. Dr. Bülend Ortaç

I certify that I have read this thesis and that in my opinion it is fully adequate, in scope and in quality, as a thesis for the degree of Master of Science.

Asst. Prof. Dr. Aykutlu Dana

I certify that I have read this thesis and that in my opinion it is fully adequate, in scope and in quality, as a thesis for the degree of Master of Science.

Assoc. Prof. Dr. Hakan Altan

Approved for the Graduate School of Engineering and Science:

Prof. Dr. Levent Onural
Director of the Graduate School

ABSTRACT

LASER SYNTHESIZED GOLD NANOPARTICLES FOR HIGH SENSITIVE STRAIN GAUGES

Salamat Burzhuev

M.S. in Materials Science and Nanotechnology

Supervisor: Assist.Prof. Dr. Bülend Ortaç

December, 2013

Recently, the conduction properties of nanoparticle films have received great deal of attention due to their unique properties attributed to quantum tunneling effect. Quantum tunneling effect, highly dependent on quantum barrier height and width, is very attractive for sensor applications. Resistive strain gauges based on gold nanoparticle (Au-NP) films show high strain sensitivity. These strain gauges are applicable for miniature applications because of its size. In addition, this nanoparticle films could be also used for various applications such as pressure and vapor sensors. Clean surfaces of laser generated Au-NPs provide high tunneling decay constant. Therefore, these films are promising for high sensitive sensor applications. In our study, the Au-NPs were directly synthesized in deionized water by nanosecond laser ablation method. The clean surface, size and aggregate clusters of Au-NPs offer advantages for high sensitivity strain sensor. We prepared Au-NPs films on flexible PDMS substrate by using hands-on drop-cast method. To obtain high gauge factor, we also investigated the nanoparticle concentration on the thin films. Laser-generated Au-NPs films demonstrated gauge factor of ~300 for higher than 0.22% strain and ~80 for the strain lower than 0.22%, which is favorably comparable to reported sensitivities for strain sensors based on Au-NPs. Mechanical characterizations for the prolonged working durations suggest long term stability of these strain sensors. We discuss several models describing conductance of Au-NP films in low and high strain regimes. To the best of our knowledge, the conduction of laser generated Au-NP films has not been studied up to date, and it is the first study that shows high strain sensitivity of these films. Au-NP films may be promising for sensor applications.

Keywords: Laser ablation, gold nanoparticles, gold nanoparticle films, quantum tunneling effect, strain gauges, nanoparticle strain gauge

ÖZET

YÜKSEK HASSAS GERİLME ÖLÇERLER İÇİN LAZERLE SENTEZLENMİŞ ALTIN NANOPARTİKÜLLERİ

Salamat Burzhuev

Malzeme Bilimi ve Nanoteknoloji, Yüksek Lisans

Tez Yöneticisi: Yrd. Doç. Dr. Bülend Ortaç

Aralık, 2013

Son zamanlarda, nanoparçacık filmlerin elektriksel iletim özellikleri eşsiz kuantum tünelleme etkisi nedeniyle büyük ilgi görmektedir. Kuantum bariyer yüksekliğine ve genişliğine oldukça bağlı olan kuantum tünelleme etkisi, sensör uygulamaları için çok cazip. Altın nanoparçacık (Au - NP) filmlere dayalı dirençli gerilme ölçer, yüksek hassasiyetli davranış göstermiştir. Bu gerilme ölçer, boyutu nedeniyle minyatür uygulamalar için uygundur. Buna ek olarak, bu tür nanoparçacık filmler, aynı zamanda, basınç ve buhar sensörleri gibi çeşitli uygulamalar için de kullanılabilir. Lazerle oluşturulan Au-NP'ların temiz yüzeylere sahip olmasından dolayı yüksek tünel bozunma özelliğine sahiptir. Bundan dolayı yüksek duyarlı sensör uygulamaları için gelecek vaat etmektedir. Bizim çalışmamızda, Au- NP'lar doğrudan nanosaniye lazer ablasyon yöntemi ile su içinde sentezlenmiştir. Au-NP'lerin temiz yüzeyleri, boyutları ve kümeleri, yüksek hassasiyet gerginlik sensörü için avantajlar sunmaktadır. Pratik damlatma yöntemi kullanılarak Au- NP filmler PDMS esnek alt-tabaka üzerinde hazırlanmıştır. Yüksek ölçü faktörünü elde etmek için, filmler üzerindeki nanoparçacıkların konsantrasyonunu araştırdık. Lazer ile oluşturulan Au-NP filmlere %0.22'den fazla gerginlik uygulandığında g faktörünün ~ 300; daha düşük gerginlikler uygulandığında ise g faktörünün ~ 80 olduğu gösterdik. Au-NP'lara dayalı gerginlik ölçen sensörler, rapor edilen hassasiyetlerle karşılaştırılabilir. Uzun çalışma süreleri için mekanik karakterizasyonlar bu gerginlik ölçen sensörlerin uzun vadeli kararlılığını göstermektedir. Biz düşük ve yüksek gerilme rejimlerinde filmlerin iletkenliğini açıklayan çeşitli modeller sunduk. Bildiğimiz kadarıyla, lazerle üretilen Au–NP filmlerin elektriksel iletimi bu güne kadar çalışılmamıştır ve bu filmlerin yüksek

gerginlik faktörüne sahip olduğunu gösteren ilk çalışmadır. Au-NP filmler sensörlerde umut verici uygulamalara yol açabilir.

Anahtar Kelimeler: Lazer ablasyon, altın nanoparçacıklar, altın nanoparçacık filmler, kuantum tünelleme etkisi, gerilme ölçer, nanoparçacık gerinim ölçer

To my mother Zhyrgal Burzhueva

Acknowledgement

I express my deepest gratitude to my supervisor Asst. Prof. Dr. Bülend Ortaç and Asst. Prof. Dr. Aykutlu Dâna. Without their guidance and supportive attitude, this thesis would not been possible.

I would like to thank Assoc. Prof. Dr. Hakan Altan for accepting to be one of my master's thesis committee members and for judgments and helpful critics.

I also would like to thank the entire Ortaç group; especially, Canan Kurşungöz for carefully reading and helping for editing my thesis.

I'm thankful to UNAM members; especially, Ongun Özçelik, Ismail Kupa, Ruslan Garifullin, Serkan Karayalçın, Sencer Ayas and Hasan Güner for being helpful and for providing productive scientific environment during the course of my M.S. degree.

I am indebted to Dr. Selim Tanriseven my science teacher, for providing first sparks in science that led to birth of my interest in this field. I'm also thankful to Daniyar Marlisov for further increasing my interest in science through my undergraduate years.

I am thankful to my friends Kanat Jakshybekov, Nurbek Kakenov, Rinat Abdurahmanov and Eldiyar Djumataev for providing wonderful atmosphere.

I owe my profound gratitude to my family. Without their love and care it would not have been possible to do any of this.

Contents

List of Figures

Chapter 1

Introduction

1.1 Nanomaterials

Nanomaterials are materials that show different properties than bulk material. Their properties strongly depend on their size. It's very interesting, because same material's properties can be tuned if precise control of size and shape is possible. These small materials can provide very unique properties that may lead to new discoveries and applications. Nanomaterials have very long history. For example; Lycurgus Cup is a 4th-century Roman glass cage cup having green color in the day light (reflected light), and red color if light is shined from inside (transmitted light). These striking properties of the Lycurgus cup appear due to Au-NPs that are in glass [1]. Immense progress in the field of nanomaterials is continuing nowadays. Nanomaterials can have unique quantum properties such as quantum confinement effect and ballistic electron transport. Quantum confinement effect can be observed in quantum dots, which are semiconductor nanoparticles, which have different optical and electrical properties than that of bulk. Ballistic electron conduction is observed in graphene in which electron mobility is very high due to characteristic of two-dimensional Dirac fermions where electrons move with relativistic speeds[2]. Also, nanomaterials show very exciting properties from the classical point of view. For example, one can obtain large surface

area from nanoparticles. Surface to volume ratio of spherical particle will be proportional to R^{-1} where R is the radius of particle; so, for nanoparticles that are just few nm (10^{-9} m) this ratio is very huge. This property of nanomaterials is useful for catalysis application because chemical reactions occur near the surface, large surface area can increase total yield of the reaction[3]. Also, if normally hydrophobic surface became nanostructured, super-hydrophobic surfaces can be obtained because high surface roughness provides high contact angle. Perhaps, best example is the lotus leaf which has a super-hydrophobic surface due to its high surface roughness[4]. On the other hand, hydrophilic surfaces present high hydrophobicity when surface roughness is increased[5]. Melting point of nanoparticles is also different from the bulk materials. It depends on the size of nanoparticles; such that the smaller the size, the lower the melting point[6].

Semiconductor nanomaterials such as quantum dots have unique properties. Their optical and electrical properties are highly dependent on their sizes[7]. When the particles become smaller than Bohr's radius, particle's properties become strongly dependent on its size [8]. This property comes from quantum confinement effect where both electrons and holes are confined in the quantum well, whose width is the diameter of nanoparticle. Generally, quantum dots are semiconductors and the band gap and size of them are inversely related to each other because of the quantum confinement effect[9]. With the current technology, it is possible to make highly controllable quantum structures[10]. Plenty of applications can be done by these quantum structures such as photodetectors [11], light-emitting diodes(LED) [12], lasers[13] and transistors [14].

Carbon based nanomaterials also show very promising properties. Most popular carbon based nanomaterials are carbon nanotubes and graphene that are composed of carbon atoms, only. Carbon nanotubes are one dimensional materials which have: very high mechanical strength[15]; and, if it is metallic, high electron mobility[16]; high thermal conductivity[17]. Generally, bundles of metallic and semiconductor carbon nanotubes mixture are observed. It is hard to separate these individual carbon nanotubes which is unfavorable for applications [17]. Graphene is one atom thick, two dimensional materials. These materials gained significant attention due to their unique electrical, mechanical and optical properties. Graphene is the strongest material; it has the highest electron mobility and it is nearly transparent [2, 18, 19].

Noble metal nanoparticles also have unique properties mainly because of their optical characteristics which depend on size, shape and dielectric constant of surrounding material. Metals have plenty of free electrons which can be oscillated when light is directed on the metal surface. Typically, this happens on the surface of metals which is in tens of nanometer order, depending on absorption coefficient. Mean free path of electrons in noble metals is $\sim 50nm$, so electrons in the nanoparticles can oscillate without scattering if electric field is applied. Collective oscillation of electrons with respect to the ions in the metal called plasmons. Absorption cross section of these particles is much higher than that absorption of quantum dots. Surface plasmons are 2D electromagnetic fields which propagate in interface between metal and dielectric. Resonance condition occurs under certain coupling regime that provides information about refractive index change. One can obtain different colors ranging from red to blue by Au-NPs with diameters between 5-100nm. Also, a surface plasmon resonance

condition depends on the shape of particle. Particularly, gold (Au) nanorods absorption spectra can be tuned by changing aspect ratio of these nanorods (Figure 1-1). [8]

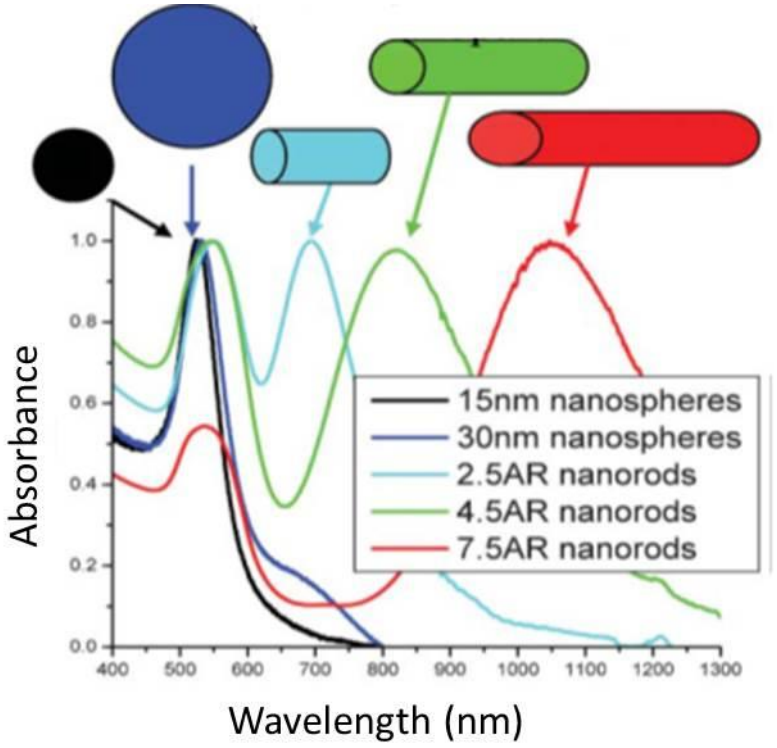

Figure 1-1 Absorption spectra of Au-NPs with different sizes and shapes.Adopted from Eustis *et al.* (2006) [8].

Noble nanoparticles can be used for sensing applications where mainly optical properties gains high interest. Applications of these nanoparticles such as Surface Plasmon Resonance (SPR) sensor and Surface Enhanced Raman Spectroscopy (SERS) are very promising. SPR sensors can be used to measure change in refractive index of a medium because SPR of Au-NPs depends on the dielectric medium. SERS is among the most popular topics because metallic nanoparticles can cause tremendous enhancing Raman signal of the absorbed molecule. This mainly happens because of large electric field enhancement near the surface of nanoparticles. [8]

1.2 Nanoparticle synthesis

Generally, nanoparticle synthesis methods can be classified as bottom-up and top-down methods. In the bottom up method, particles are built from fundamental building blocks such as atoms and molecules. This method generally requires less energy than top-down method. There are several methods which may be categorized as bottom-up method such as chemical vapor deposition (CVD), molecular self-assembly, sol-gel processes, electrodeposition, and so on[20]. Noble nanoparticles are generally synthesized by Turkevich method which was developed in 1951. In this method, Au and citrate is mixed in water where temperature, ratio of Au to citrate and amount of reagents govern nanoparticle size distribution[8].

In top-down method, the particle is made from bulk material by reducing its size. This technique generally requires more energy because of the binding energy of atoms in the bulk. Optical and e-beam lithography are very convenient fabrication methods that can be categorized as top-down methods[8]. In these methods, light and electrons are used to make patterns on the the surface. Due to diffraction limit, optical lithography cannot achieve small feature size. On the other hand, one can achieve small feature size by using e-beam lithography which is relatively an expensive technique. Other methods such as thermal evaporation, e-beam evaporation, laser ablation, arc-discharge method are also widely used[20].

1.3 Nanoparticle synthesis by laser ablation in liquids

Laser ablation is the material removal by focusing the laser light on the surface of target material. Laser light leads to heating of material causing material removal by vaporization, plasma generation, melting and fragmentation[21]. Commonly, pulsed

lasers are used for ablation in order to heat only irradiated area, not the whole surface, to prevent heat diffusion. Generally, shorter pulses lead to smaller heated area [22]. Laser ablation in liquid is another top down method for production of colloidal solution. In this method, nanoparticles are generated by focusing laser light on target material that is in the liquid medium. Interestingly, removed materials from the target can form nanoparticles. This method provides several advantages for nanoparticle synthesis. A main advantage of this method is that experimental setup is relatively simple, while it can provide synthesis of wide range of nanomaterials. Parameters of experimental setup can be classified as laser parameters and target parameters. Laser parameters are pulse duration, fluence (pulse energy divided by spot area), wavelength, repetition rate, number of pulses[21]. Target parameters are the type of the bulk target, type of the liquid and temperature of the system. Variety of nanomaterials can be obtained by laser ablation such as metals[23], metal oxides[24], noble metals[25], semiconductors[26].

Also, nanoparticles can be generated without surface ligands that may be valuable for several applications. Clean surfaces of these nanoparticles may be advantageous for several applications and if needed may be functionalized further.

1.4 Nanoparticle strain gauges

Strain gauges are used to convert mechanical deformations to electrical signals. Recently, conduction of Au-NP film was extensively studied. Conduction behavior of this film strongly depends on length of the linker molecules [27, 28]. After some time, researchers realized that Au-NP films can be used as sensitive strain gauges [29, 30]. High strain sensitivity of these sensors depends on tunneling decay constant that is

dependent on linker molecule[29]. Also, sensitivity can be increased by increasing size of nanoparticles or aggregates[29].

Laser generated nanoparticles have high tunneling decay constant simply because they do not have any linker molecules. In addition, nanoparticle size and aggregation of laser generated nanoparticle maybe advantageous for high strain sensitivity.

1.5 Organization of thesis

In the chapter 1, introduction to nanomaterials and its synthesis was discussed. Also, a very brief explanation provided about the laser ablation method and nanoparticle strain gauges. In chapter 2, we have discussed about laser ablation method. Laser heating; material ejection from target; and nanoparticle growth were briefly discussed. In the third chapter of this thesis, we described the synthesis of Au-NP by laser ablation method. Then, these nanoparticles were characterized by transmission electron microscope (TEM), absorption spectroscopy and X-ray photoelectron spectroscopy (XPS) for determining size and surface chemistry of these nanoparticles. In chapter 3, strain gauge working principles and basic requirements of these sensors are discussed. Basic explanation of Au-NP strain gauge together with brief literature overview is also given. In chapter 4, the description of laser generated Au-NP film fabrication by simple drop-cast method is given. Mechanical characterizations of these films reveal high strain sensitivity and moderate repeatability. We also develop numerical models to better understand the conduction behavior of Au-NP films. In the chapter 5, a brief summary of thesis and outlook is provided.

Chapter 2

Laser ablation method, nanoparticle synthesis and experimental results

2.1 Ultra short pulsed laser ablation

Laser ablation is material removal by irradiating the laser light on the material. When the laser is shined on the surface of materials, due to electromagnetic nature of light electron clouds starts to oscillate, and electrons gain kinetic energy, then energy is transferred to lattice [31]. Particularly, in metals, light is absorbed mainly by free electrons. High amount of evaporation of metal occurs when lattice energy exceeds evaporation specific heat leading to ejection of material from the surface[22].

Evaporation of metals due to laser was intensively studied[32, 33]. Special attention gained by nanosecond, picosecond and femtosecond laser was gained due to presence of different evaporation regimes [31, 34]. Laser ablation was explained by two temperature model[35, 36]. In this model, temperatures of electron and lattice taken separately as T_e and T_l. Two temperature one dimensional model is given by following equations 2.1, 2.2, 2.3, 2.4:

$$C_e \frac{\partial T_e}{\partial t} = -\frac{\partial Q(z)}{\partial z} - \gamma(T_e - T_l) + P \qquad 2.1$$

$$C_l \frac{\partial T_l}{\partial t} = \gamma(T_e - T_l) \quad 2.2$$

$$Q(z) = -k_e \frac{\partial T_e}{\partial z} \quad 2.3$$

$$P = I(t) A \alpha e^{-\alpha z} \quad 2.4$$

where C_e and C_l are heat capacities (per unit volume) of electron and lattice; z-direction of laser light to the metal; P- is laser heating term (W/cm^3); γ- electron-lattice coupling constant; k_e- electron thermal conductivity; $Q(z)$- heat flux; $I(t), A$ and α are laser intensity, surface absorptivity and absorption coefficient of material, respectively[31]. Heat capacity of lattice is much higher than heat capacity of electrons which allows electrons heated for very high temperatures. If electron temperature remains smaller than Fermi energy($k_b T_e < E_f$) ,where k_b and E_f are Boltzmann constant and Fermi energy, heat capacity of electron is proportional to temperature ($C_e = CT_e$ where C is constant)and non-equilibrium electron thermal conductivity is $k_e = k_0 T_e / T_l$ where $k_0(T_l)$ is equilibrium thermal conductivity of metal. These equations have three different regimes which depend on $\tau_e = C_e/\gamma$, $\tau_l = C_l/\gamma$ and τ_L which are electron cooling time, lattice heating time and laser pulse duration.[37]

For femtosecond pulses $\tau_L \ll \tau_e$, electron-lattice coupling coefficient can be neglected as $\frac{C_e T_e}{t} \gg \gamma(T_e)$. Electron heat conduction term may be neglected in order to simplify equations. $D_e \tau_L < \alpha^{-2}$. [37]

After solving these equations, ablation depth can be found. Evaporation can be explained by equation 2.5:

$$V = V_0 \exp(-\frac{\rho\Omega}{C_l T_l}) \qquad 2.5$$

where ρ and Ω are density and the specific heat of evaporation of metal; V is the velocity of the evaporation front and $V_0$is a constant depending on the material. Ablation depth per pulse is $L \cong \frac{1}{\alpha}\ln\left(\frac{F_a}{F_{th}}\right)$where F_a is absorbed laser fluency; $F_{th} \cong \rho\Omega/\alpha$ (ρ and Ω are density and the specific heat of evaporation of metal (per unit mass)) threshold laser fluency needed to evaporation with femtosecond laser pulses. This type of regime maybe advantageous for micro structuring as heat does not have enough time to diffuse so that smaller area can be evaporated[37].

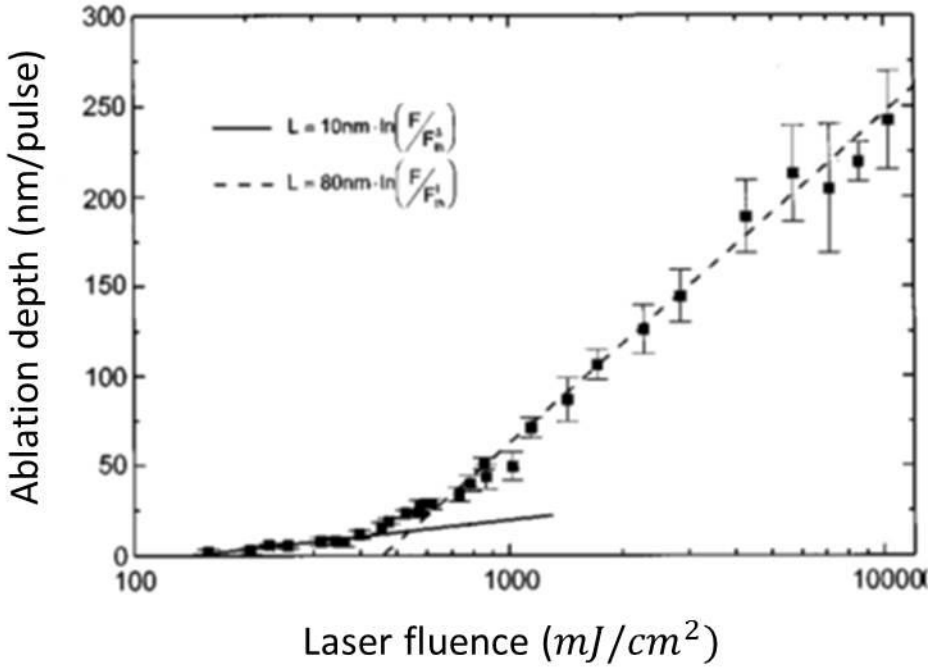

Figure 2-1 150-fs laser pulses are used to ablate copper. Ablation depth per pulse versus laser fluence is shown where ${F^{\delta}}_{th} = 140\ mJ/cm^2$and ${F^{l}}_{th} = 140\ mJ/cm^2$corresponding to fits. Adopted from Nolte *et al.* (1997) [31].

Femtosecond laser ablation depth per pulse versus depth is shown in the Figure 2-1. Experimental results are fairly same with the theoretically predicted results. However, in the Figure 2-1 , two fits for femtosecond laser ablation results are shown. The first one corresponds to the fit which was explained above where optical penetration of material is $\alpha \cong 10\ nm^{-1}$ which is nearly in agreement with well-known optical penetration depth. In the second fit, optical penetration depth is assumed to be changed ($l \cong 80\ nm^{-1}$)because of high fluence. [31]

For the picosecond pulses following conditions are satisfied $\tau_e \ll \tau_L \ll \tau_l$. Under certain assumption ablation depth can be found same as for the femtosecond pulses. However, in this regime electron heat conduction term was neglected which is not very appropriate assumption as electron heat conduction is in orders of picoseconds[38] .

For nanosecond pulses, $\tau_L \gg \tau_l$, so we can assume that electron and lattice temperatures are same which simplifies equations 2.6.

$$C\frac{\partial T}{\partial t} = -\frac{\partial}{\partial z}(-k\frac{\partial T}{\partial z}) + I(t)A\alpha \mathrm{e}^{-\alpha z} \qquad 2.6$$

Heat penetration depth can be shown by $l \sim \sqrt{Dt}$, where D is heat diffusion coefficient ($D = k_0/C_l$). This regime is studied by several groups[33, 39]. In this regime, light energy first melts metal and then evaporates it. The energy absorbed by metal per unit mass is $E \sim \frac{It}{\rho l}$; so, after certain $t = t_{th} = D(\Omega\rho/\mathrm{I})^2$, the energy is greater than the

specific heat of evaporation. Condition for strong evaporation is $F > F_{th} \sim \rho\Omega\sqrt{D\tau_L}$ [34]. For the nanosecond regime heat is propagated along the metal which leads to evaporation of larger layer than in previously explained regime.

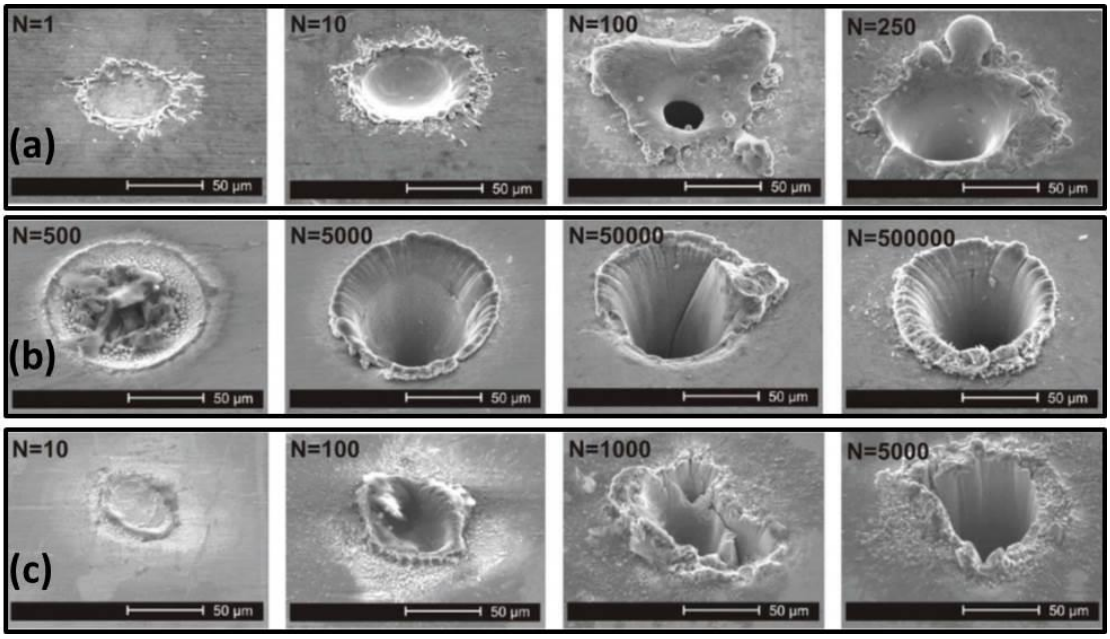

Figure 2-2 SEM images of (a) nanosecond, (b) picosecond and (c) femtosecond laser ablation of iron. Adopted from Leitz *et al.* (2011) [40].

While picosecond and femtosecond lasers provide higher precision[31, 34, 40] as can be seen from the

Figure 2-2, nanosecond laser provides higher ablation yield[40] because nanosecond laser systems have higher power than picosecond and femtosecond laser pulses.

2.2 Nanosecond pulsed laser ablation

In the section 2.1, nanosecond pulsed laser heating process was described, while ablation mechanism was just touched. Material removal process and nanoparticle generation is further studied in this section.

2.2.1 Thermal process of nanosecond laser ablation

Miotello *et al*. (1999) explained ablation of material by normal vaporization, normal boiling, and phase explosion [41]. Vaporization occurs when a material changes its state from condensed state to vapor state. There is no threshold in vaporization which occurs on the surface. Vaporization which includes evaporation and sublimation near the boiling point can be explained by Hertz-Knudsen equation 2.7:

$$flux = \frac{\alpha(P - P_0)}{\sqrt{2\pi k_b T}} \ particles/m^2 s \qquad 2.7$$

where α, P, P_0 and k_b are condensation coefficient , equilibrium vapor pressure, ambient pressure and Boltzmann constant. Evaporation and sublimation occurs only in the surface of the condensed matter. On the other hand, normal boiling and explosive boiling present inside material. According to Miotello *et al*. (1999), normal vaporization doesn't occur under short pulse ($< 1\ ns$) ablation while $100\ ns$ pulse is sufficient[41].

Boiling is a fast vaporization and occurs when vapor pressure exceeds surrounding pressure. Normal boiling is similar to water boiling process that we face in our daily life. In normal boiling bubbles appear and temperature of water doesn't change upon heating process. Both normal vaporization and normal boiling follows bimodal decomposition in which gas and liquid exists in equilibrium. Nucleation of the bubbles is heterogeneous during this process[41].

Phase explosion appears when material is suddenly superheated above boiling point near to critical thermodynamic point. In this regime spinodal decomposition and homogeneous nucleation of bubbles occurs[41]. Phase explosion is also commonly called "explosive boiling" of metals studied by Martynyuk *et al.* (1974) [42]. First,

explanation of phase explosion of metals by intense laser light was proposed by Martynyuk [43]. By studying metal vaporization on microsecond time scales by laser pulses and electrical explosion of wires, they estimated critical temperature. In this study, he concluded that phase explosion will not present in the $1\,ns - 100ns$ light pulses. However, recent studies demonstrate that phase explosion is main mechanism of material removal for $1\,ns - 100ns$ [41, 44]. While, normal boiling is not a significant ablation mechanism in $1\,ns - 100ns$ pulsed lasers since bubble diffusion process is very slow[41]. Bulgakova *et al*. (2001) have shown that there are threshold fluences for explosive boiling processes (Figure 2-3).

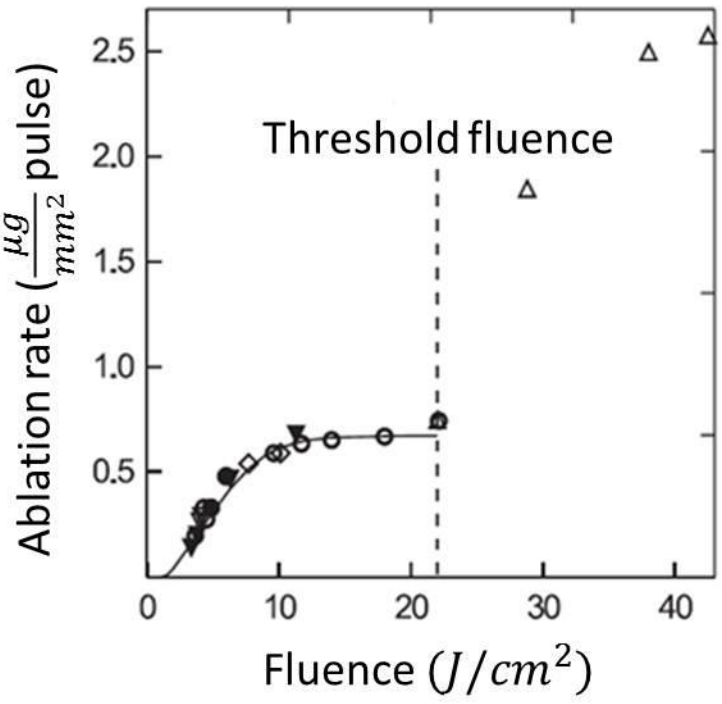

Figure 2-3 Ablation rate per pulse versus laser fluence graph of the graphite. Theoretical estimation are shown by solid line and dashed line is treshould fluence. Ablation is performed by Q-switched Nd-YAG laser (1064 nm wavelength, 13 ns pulse duration) under vacuum conditions ($10^{-3}\ Pa$). Adopted from Bulgakova *et al.* (2001) [44]

2.2.2 Plasma generation and other processes

In order to understand whole picture of ablation, it is important to understand other process which take place during ablation such as photoionization, photomechanical stress and especially plasma generation. In the femtosecond laser ablation of polytetrafluoroethylene near the threshold fluence, emission of high-energy ions was observed. This can be described by columbic explosion due to photoionization process [45]. Asashi *et al*. studied laser ablation of organic microcrystals (quinacridone) where they observed photothermal ablation for nanosecond laser, and photomechanical process for femtosecond laser[46]. Because of photoionization and heating of the target, plasma plume can be generated. Plasma plume is a forth state of matter. Plasma is ionized gas composed of a lot of positively and negatively charges so that it can influence gas electrical behavior which is distinct from gas behavior. For nanosecond pulsed lasers, plasma plume life time is about twice of the pulse duration[47]. So, for nanosecond lasers light can be reabsorbed by plasma resulting in larger ablated area. On the other hand, with the picosecond and femtosecond regime, this will not happen. Plasma plume generated by laser ablation temperature and pressure are in the orders of several 10^3 K and several GPa [44, 48, 49]. Below the plasma regime ablation yield in liquid environment is slower than in vacuum because liquid confines solid[50]. However, when ablation regime above plasma threshold, ablation yield is higher in the liquid than in the vacuum because there is more confinement of plasma in the liquid [51]. Plasma releases its energy to liquid which generates cavitation bubble. Cavitation bubble expands and travels with the speed several times higher than sonic speed, having maximum radius in the order of

millimeters [51, 52]. Expansion of cavitation bubble leads to decrease in temperature and pressure become smaller than surrounding pressure. These processes lead to the collapse of bubble by emission of a shock wave.

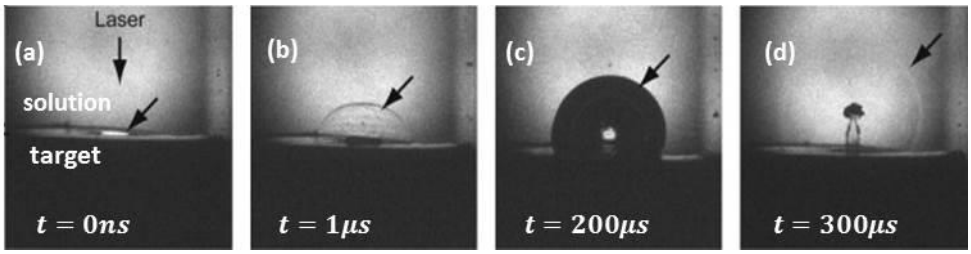

Figure 2-4 Shadowgraph images of cavitation bubble expansion during laser ablation of silver in 18 mM PVP solution. Various phenomena are observed: a) optical emission, b) shockwave, c) cavitation bubble, d) secondary shockwave [51].

2.3 Formation of nanoparticles

Due to complexity of laser ablation process, several nanoparticle formation mechanisms will occur. During ablation process, the material is removed by vaporization, melting, fragmentation [53, 54]. For low nanosecond laser fluencies, normal vaporization is the main mechanism of material removal in laser ablation. Vaporized particles will nucleate and then coalescence and growth of nanoparticles will be observed [55]. Bulgakova *et al.* explained that main ablation mechanism during nanosecond laser ablation is due to explosive boiling under high fluences. For subthreshold fluences of laser, material ejection will be due to vaporization where vaporized atoms and melted droplets may appear[44]. For even higher fluencies amount of melted droplets can be increased further as well as fragmented particles appear, too. Researchers observed that size distribution of laser generated nanoparticles can be fitted to log normal function and some studies show that two modes can be

observed both for nanosecond and femtosecond pulsed laser ablation [56, 57]. Two modes may appear due to two different ablation mechanisms involved where normal vaporization is responsible for smaller particles while explosive boiling is the larger ones. In both of the studies, distribution of second mode – larger particles - is increased by increasing laser fluence [56, 57]. If the melted and fragmented particles are already detached from the surface, then nucleation may not be important because those particles already form nuclei, which are directly obtained during laser ablation process [21].

Most of the ablated nanoparticles are polycrystalline which means that nuclei coalescence should occur [55]. Generally, particles obtained by laser ablation have spherical shape meaning that nuclei coalescence may occur when lattice rearrangement occurs for decreasing interface energy. Also, there are several evidences that nanoparticle size is decreased when stabilizing agents such as polyvinylpyrrolidone (PVP) and sodium dodecyl sulfate (SDS), are used [51, 58]. So, growth of nanoparticle after ablation occurs.

Tsuji *et al.* (2003) investigated nanosecond pulsed laser ablation mechanism by microsecond-resolved shadowgraphy for Ag, Au, and Si targets. He observed cavitation bubble and straight jet generation where cavitation bubble is generated due to plasma (Figure 2-5). Straight jet's ejection velocity and appearance were very distinct from cavitation bubble. Therefore, they conclude that straight jet generation may be due to ejection of clusters and droplets from the target[59].

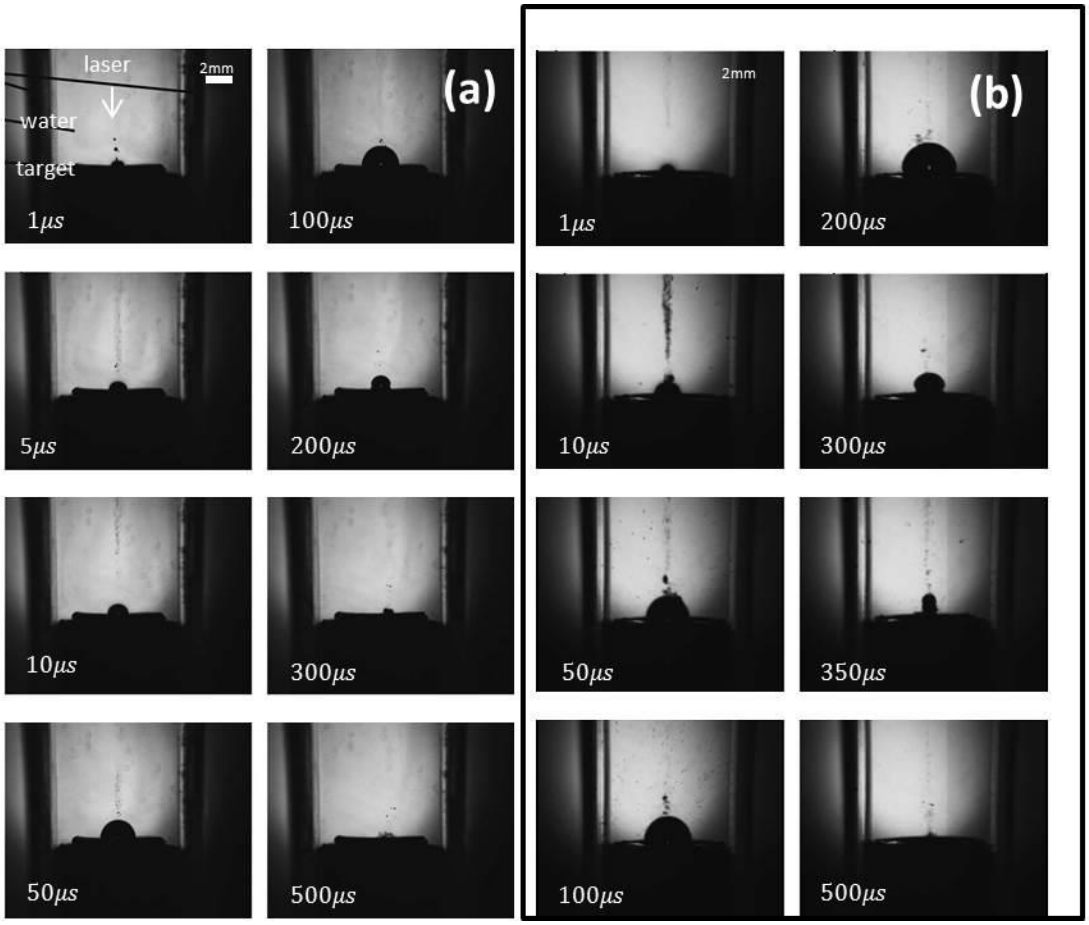

Figure 2-5 Shadow graph pictures at various delay times of laser ablation of silver in water at laser fluences (a) $18J/cm^2$ and (b) $36J/cm^2$. Adopted from Tsuji *et al.* (2004) [59].

One can consider combination of thermal effects and plasma effect on nanoparticle growth under high fluences. Nanoparticle generation will mainly depend on laser fluence. After certain threshold fluence explosive boiling will occur. These nanoparticles will mostly be formed by means of melted and fragmented particles; while, under lower fluences nanoparticle growth will be mainly due to vaporized atoms. However, combination of vaporized, melted and fragmented particle influence on nanoparticle formation can also be considered. In this case, vaporized, melted and fragmented particles all contribute to the growth of nanoparticle. In Figure 2-6, vaporized atoms can nucleate, coalesce, and grow for the nanoparticle formation. In addition, vaporized atoms can attach to surface of melted or fragmented particles resulting in the increase of particles' size. Moreover, coalescence of melted particle may occur when their temperature is high enough. Fragmented materials may change its shape due to high temperature which will reduce its surface energy.

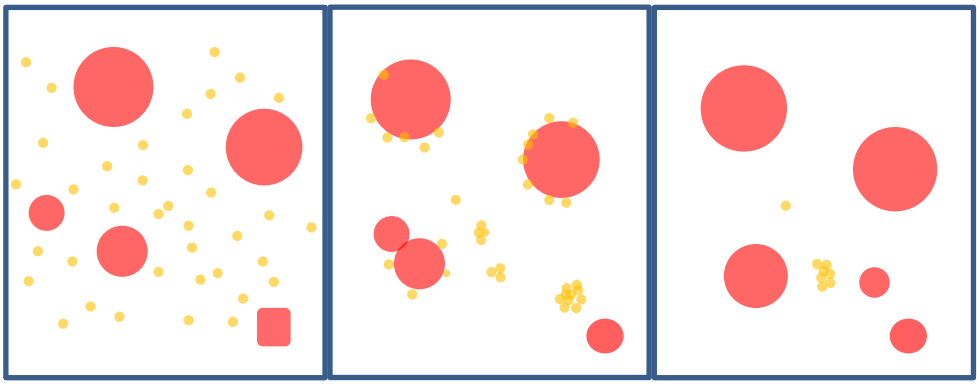

Figure 2-6 Schematic representation of growth of nanoparticles when vaporized atoms (yellow balls), melted drops (red balls) and fragmented (red rectangle) particles exist in the solution. Note that dimensions are not to scale.

2.3.1 Wavelength and fluence effect on nanoparticle formation

Researchers have shown that laser fluence play important role on size distribution and structure of particles [57, 60]. Nichols *et al*. have well explained the experimental results of nanosecond pulsed laser ablation of platinum (Pt) in water where the specific parameters, such as laser wavelength and fluence effects on nanoparticle size, structure and chemical composition, were studied [25, 56, 60]. They have used Nd:YAG laser operating at wavelength $1064,\ 532$ and 355 nm with the pulse duration $10,\ 8$ and $7\ ns$, respectively. In this study, they have observed that surface of ablated Pt target have distinct properties for different operation wavelength. When targets are ablated by $355\ nm$ and $1064\ nm$ laser light, shallow ripples and large craters ($20\mu m$ diameter) are observed on the surface, respectively (Figure 2-7). On the other hand, when these targets are ablated by $532\ nm$ laser light, both shallow ripples and large craters appear on the same surface [25]. Because 355 nm light is strongly absorbed by generated nanoparticles, the fluence delivered to the target through colloidal solution is dramatically decreased while 1064 nm laser light is delivered much more to the target. For high enough fluences of nanosecond lasers explosive boiling may be responsible for material removal [41] which maybe the reason for observing such differences.

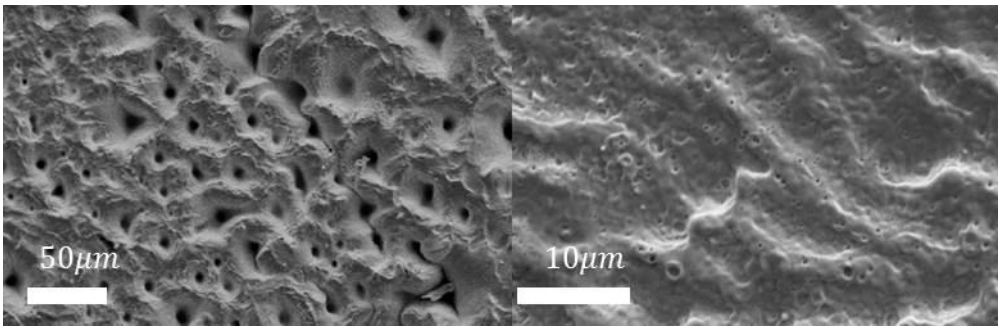

Figure 2-7 Platinum surface image after ablation with 1064 nm and 355 nanosecond laser with fluences $42\,J/cm^2$ and $65\,J/cm^2$. Adopted from Nichols *et al.* (2006) [25].

Mass yield of ablated material is largest for $1064\,nm$ laser for fluences $> 10\,J/cm^2$ [56]. Tsuji *et al*. synthesized silver nanoparticles by laser ablation and studied wavelength dependence of mass yield and mean sizes [61-63]. He has also found that more nanoparticles can be obtained by 1064 nm laser light than the ones with 355 nm laser light which is focused on silver target when the light fluence is $12\,J/cm^2$. On the other hand, when optical fluence of laser is $908\,mJ/cm^2$, more nanoparticles were produced by 355nm laser than 1064 nm laser [62]. These results are fairly consistent with the results of Nichols *et al*. as shown in the Figure 2-8. Nichols *et al*. (2006) explained that under low laser fluences ablation yield is determined by absorption coefficient; however, this cannot explain Tsuji *et al*. results (absorption coefficient of silver is higher for 1064nm than 355 nm light [64]). Indeed, this discrepancy can be explained by combination of reflectivity and absorption coefficient on the ablation yield. Reflectivity of Pt for 1064 nm light is higher than 355nm light; therefore, ablation yield for low laser fluences is higher for 355 nm light than 1064 nm. For higher laser optical fluences (>$10\,J/cm^2$) more nanoparticles are

generated by longer wavelength because generated nanoparticles strongly absorb shorter wavelength resulting in decrease of delivered laser fluence to the target. For high enough fluences of nanosecond lasers explosive boiling is responsible for material removal [41] which maybe the reason for observing such differences.

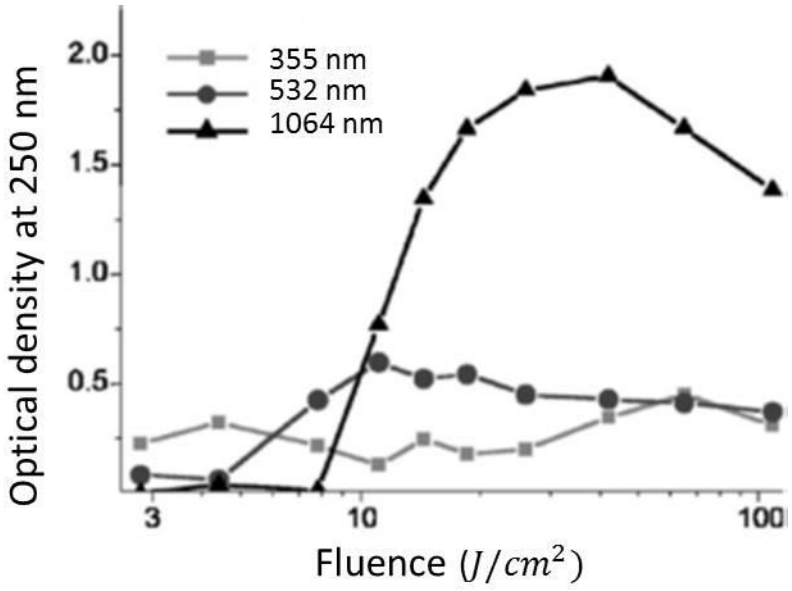

Figure 2-8 Ablation yield versus laser fluence at different wavelength which is measured by the optical density at 250 nm of platinum colloidal solution. Adopted from Nichols *et al.* (2006) [56].

Particle sizes and size distributions also depend on operation wavelength because absorption of generated depends on wavelength. Two distinct modes of size distribution are observed which are fitted as a log-normal distribution. First mode is suggested to be due to thermal vaporization; and second mode is due to explosive vaporization. Laser ablation of Pt with 1064, 532, 355 nm nanosecond lasers under $10 - 70\, J/cm^2$ light fluences reveal spherically shaped and nonagglomerated nanoparticles with the size range $1 - 30\, nm$ [56]. On the other hand, when the fluence

of 335 nm laser is less than $10\ J/cm^2$ amorphous, gel-like, globular particles are found in the size range of $20 - 200\ nm$ [60]. At fluencies higher than $70\ J/cm^2$ for the same laser, gel-like materials are also observed and Pt nanoparticle number decreases while larger particles appear more frequently[60].

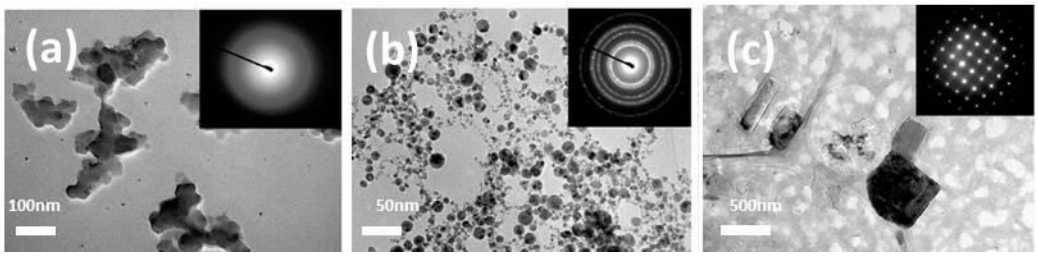

Figure 2-9 TEM images of laser synthesized platinum nanoparticles by 355 nm wavelength with laser fluences a) $4\ J/cm^2$, b) $26\ J/cm^2$ and c) $110\ J/cm^2$. Selected area diffraction images are shown in insets. Adopted from Nichols *et al.* (2006) [60].

2.4 Experimental results of laser synthesized Au-NPs in deionized water

2.4.1 Experimental setup of laser ablation in liquid

Au-NPs were obtained by laser ablation in deionized water. Au block (99.999%, Kurt J. Lesker) was cleaned by sonification in acetone prior to laser ablation without any additional purification. The generation of colloidal nanoparticles from Au block was carried out using a commercial pulsed Nd:YLF laser (wavelength: λ= 527 nm, 16 W average power, pulse duration t= 100 ns, pulse energy E= 16 mJ for 1 kHz). The cleaned Au block was placed in a glass vessel containing 23.5 mL of pure deionized water. The laser beam was focused on the target by using a plano-convex lens with focal length of 50 mm. The height of liquid layer over the Au target is ~5

mm. The laser ablation was carried out for ~10 min, and the laser beam is scanned over the target surface. During the laser ablation, the formation of colloidal nanoparticle solution with dispersed Au-NPs in liquid media was observed as a color change of the deionized water. After the laser irradiation, the color of the Au-NPs solution became dark-red. Basic experimental setup is shown where laser light is focused on the target material which is in the liquid in the Figure 2-10.

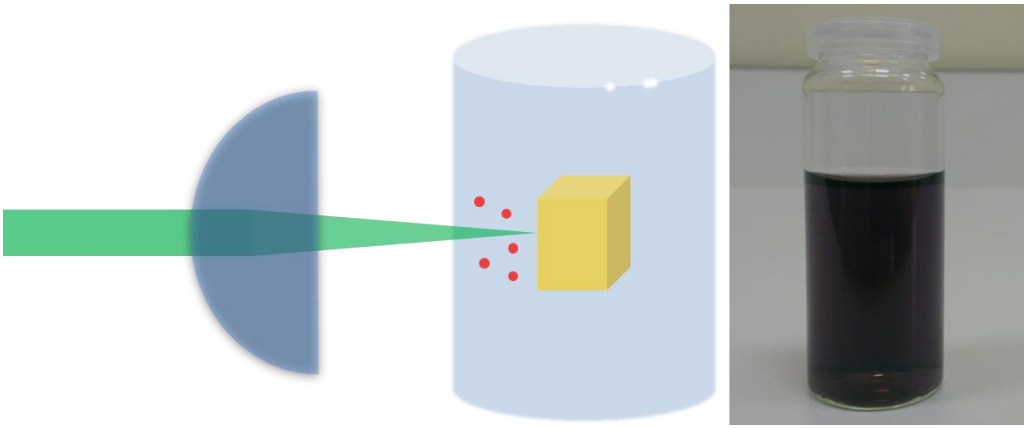

Figure 2-10 Schematic presentation of laser ablation in liquids and obtained Au-NP colloidal solution.

2.4.2 Characterizations of laser synthesized Au-NPs

Transmission electron microscope (TEM) is an imaging technique that uses electrons to image specimen. Electron source of TEM is typically tungsten which is connected to high voltage source up to 100-200 keV; so, electrons are emitted by means of field emission and thermionic emission. In order to focus electrons, magnetic lenses are used. Abbe diffraction limit is defined as $d = \frac{\lambda}{2nsin\theta}$ where λ is wavelength of light, nsinθ is numerical aperture (n-refractive index, θ- half angle of maximum light angle that can enter lens). So, in the air, maximum resolution of optical microscope is approximately half of the wavelength (about 550nm) which is ~ 225 nm. On the other

hand, electrons have very small wavelength compared to visible light wavelength. Wavelength of electron can be calculated by using de Broglie relation which is $\lambda = h/\sqrt{2meV}$ where m is mass of electron, e is electron charge, V is applied voltage, and h is Planck's constant. So, if applied bias is in 100 keV, electron wavelength is ~ $0.5\ 10^{-11}$ m. For $\theta = 10^{-2}$ radians, resolution can be calculated by above given diffraction limit formula which is$\sim 0.5\, nm$. However, practical resolution limit of TEM is generally due to aberrations and distortions. TEM is the ultimate technique for nanoparticle imaging. Because electrons have very short wavelength, it is possible to see even crystal structure of nanoparticles. The structure of Au-NPs generated by nanosecond pulsed laser ablation were studied by TEM (TEM model FEI – Tecnai G2F30) system.

TEM sample was prepared by drop-casting solutions onto carbon-coated TEM grid. Representative TEM image of the Au-NPs is shown in Figure 2-11 (a), showing well dispersed spherical NPs. Size distribution of Au-NPs is given in Figure 2-11 inset. An average nanoparticles size of 13 nm is seen, with a distribution covering the range from 2 nm to 25 nm. Although, TEM is direct evidence of nanoparticle existence, this technique lacks for statistical analysis. TEM images are taken from very small area due to high magnification. Therefore, absorption spectroscopy should be applied in order to compare results.

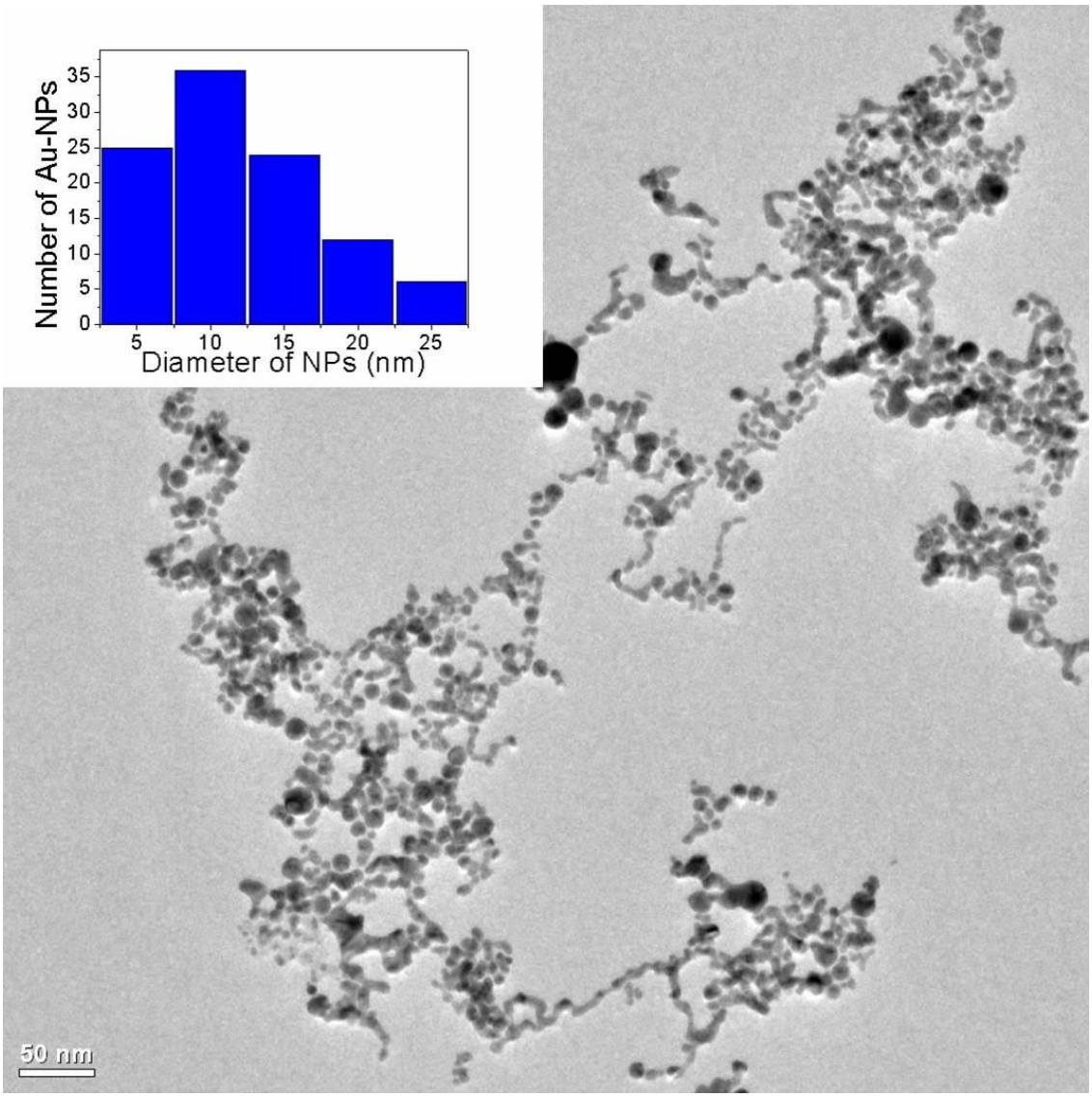

Figure 2-11 TEM image of Au-NPs. The inset shows the histogram of size distribution calculated from TEM images.

XPS is widely used for surface analysis which measures elemental composition; chemical state of element; relative composition of constituents; and valence band structure. When target is irradiated by X-Ray, electrons are ejected from the surface by

means of photoelectric effect. By measuring amount and kinetic energy of electron, binding energy of electrons can be calculated. As binding energy of electron is unique for every element, it is possible to determine chemical composition of target surface. The surfaces of nanoparticles play a key role on the quantum tunneling effect. The elemental composition and the chemical state of the Au-NPs were studied by XPS. The XPS data were recorded with Au-NPs samples placed on silicon substrates. XPS measurements were performed on a monochromatic K-Alpha instrument (Thermo) operating at 12 kV and 2.5 mA. XPS spectra were collected with a photoelectron take off angle of 90° from a 200 μm diameter circular spot on the sample surface plane, energy steps of 0.1 eV, and pass energy of 30 eV. The control of the flow of the electrons to the surface is achieved by means of a well-controlled flood gun technique. XPS spectrum in the Figure 2-12, present two peaks located at 84.0 eV and 87.7 eV corresponding $4f_{7/2}$ and $4f_{5/2}$ [65, 66]. XPS spectrum reveals that the surface of Au-NPs is in low oxidation state. Thus, tunneling decay constant is higher than those particles which have surface ligands. Higher tunneling decay constant is significant for obtaining more sensitive strain gauges [29].

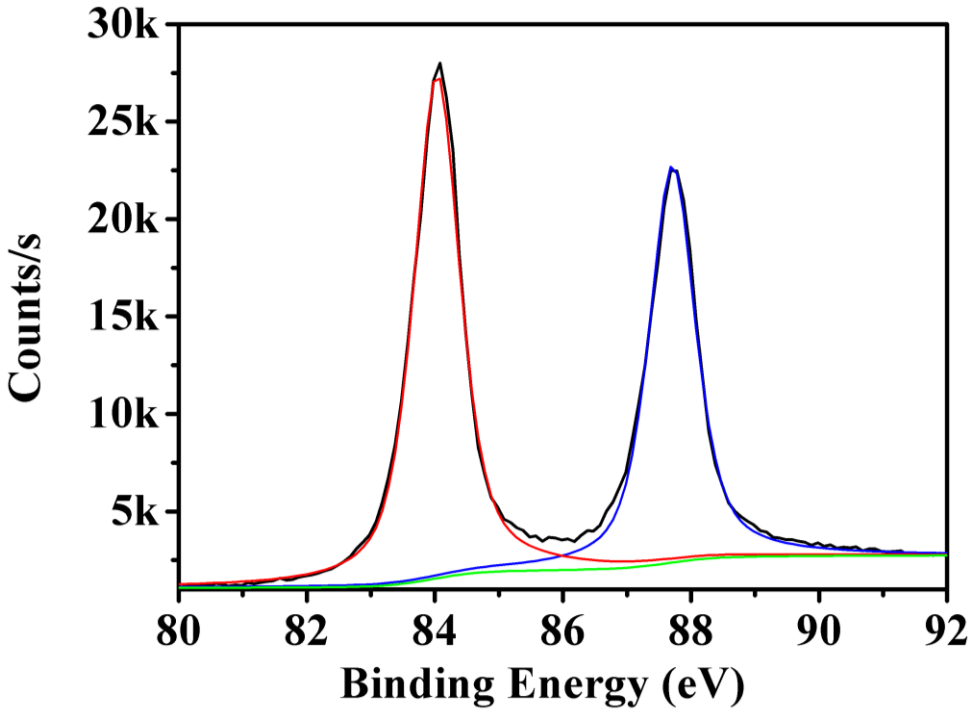

Figure 2-12 XPS spectrum of Au-NPs. Two peaks correspond to $4f_{7/2}$ and $4f_{5/2}$ binding energies.

UV-Vis spectroscopy is used measure absorbance of colloidal solution. This technique measures absorbance or reflection of solid and liquid samples from near-ultraviolet to near-infrared region. UV-Vis spectroscopy measures absorption of the specific wavelength by using Beer-Lambert law. Cary 5000 UV-Vis-NIR Spectrometer was used to measure absorbance of Au-NPs solution. Absorption measurements with the baseline correction are performed between 200nm and 800nm. In the Figure 2-13, absorption peak appears at 520 nm due to surface plasmon resonance of Au-NPs condition at this wavelength. Plasmon peak is not sharp because nanoparticle size distribution is broad as also can be seen from the TEM picture. UV-Vis spectroscopy is very convenient technique for size and shape determination of Au-NPs. Au-NPs

present unique absorption spectrum because of surface plasmon resonance condition. This technique provides statistical information about particles size where absorption is obtained from whole colloidal solution; while, TEM images only shows particles in the small area.

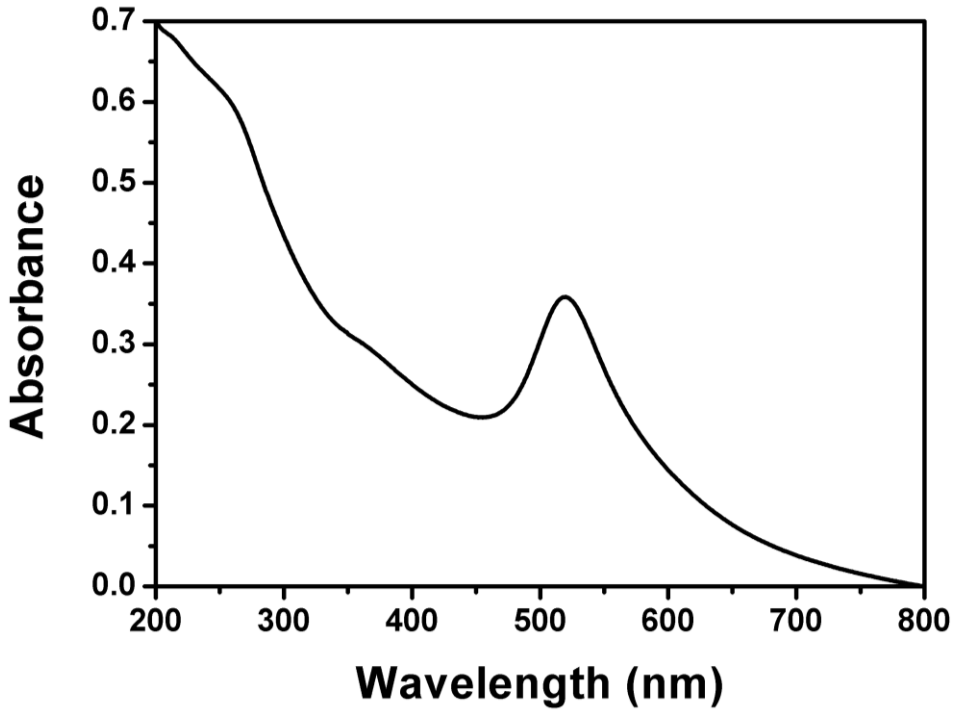

Figure 2-13 Absorbance spectrum of Au-NP colloidal solution

Chapter 3

Strain gauge

3.1 Conventional strain gauges

Strain is the change in length of material when force is applied. It is equal to fractional change in length of the material (equation 3.1).

$$\varepsilon = \frac{\Delta l}{l} \qquad 3.1$$

Strain gauges are used to sense the strain. They can be also used in other types of sensors such as motion sensors, accelerometers, force and pressure sensors. Generally, strain gauges are used to measure resistance change when strain is applied which are called piezoresistive gauges. There are several types of piezoresistive strain sensors such as liquid, metal foil, semiconductor strain gauges.

3.1.1 Liquid strain gauge

In order to describe how strain sensors work, it is better to begin with liquid (mercury) strain gauges. These strain gauges are used to measure blood pressure. Resistance of the liquid strain gauge is changed while applying strain, because length is increased and cross sectional area decreased (Figure 3-1).

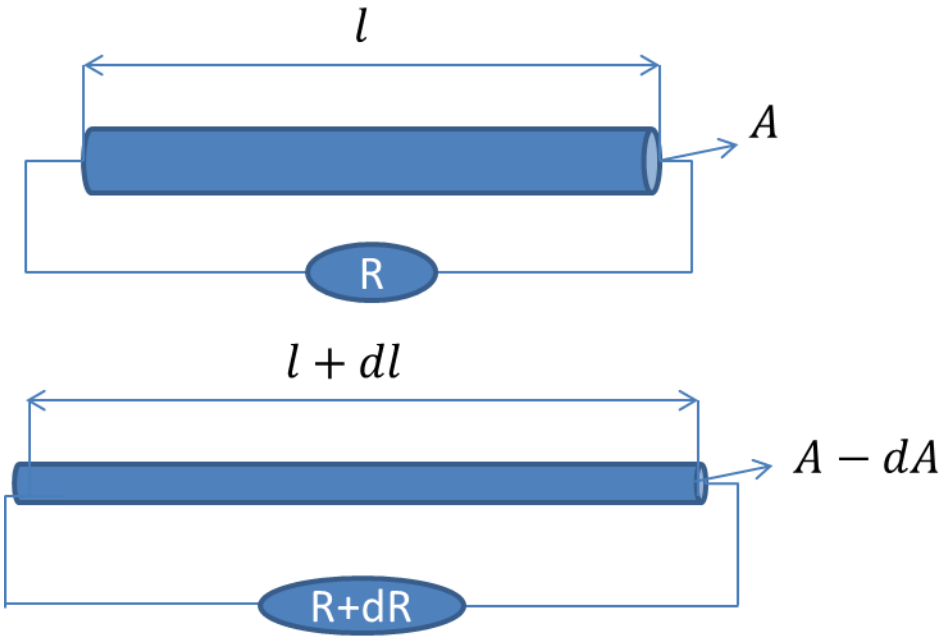

Figure 3-1 Schematic representation of strain gauge working principle

Mercury doesn't compress and change its resistivity when strain is applied. Resistance is proportional to resistivity, length of material and inversely proportional to cross section area (equation 3.2). So, fractional resistance change of liquid strain gauge can be derived by using the equations 3.2, 3.3 and shown by equation 3.4 where R, ρ, l, A, V, ε, and g are resistance, resistivity, length, cross sectional area, volume, strain, and gauge factor.[67]

$$R = \frac{\rho l}{A} = \frac{\rho l^2}{V} \qquad 3.2$$

$$dR = \frac{2\rho l dl}{V} = \frac{2R dl}{l} \quad 3.3$$

$$\frac{dR}{R} = 2\varepsilon \quad 3.4$$

Sensitivity of strain gauge is shown by gauge factor which is proportional to fractional resistance change divided by strain (equation 3.5)[67].

$$g = \frac{\frac{dR}{R}}{\frac{dl}{l}} \rightarrow \frac{dR}{R} = g\varepsilon \quad 3.5$$

Therefore, gauge factor has fundamental limitation for liquid strain gauges; gauge factor is equal to 2 (equation 3.4). If 0.2 % strain is applied to mercury strain gauge, resistance is changed by only 0.4 %.

3.1.2 Metal foil strain gauges

For metal foil strain gauges, which are most widely used strain sensors, we need to take in account that material is compressed and changed its resistivity while strain is applied. Basic principle of metal foil strain gauge is shown in the Figure 3-2, which is nearly same as liquid strain gauge. Equation 3.6 can be used to describe resistance change where D and ϑ are diameter and Poisson's ratio. Poisson's ratio is proportional to fractional change in diameter of cross section area divided by strain which is generally 0.2~0.4 for metals [67].

$$R = \frac{\rho l}{A} = \frac{4\rho l}{\pi D^2} \tag{3.6}$$

Now, by using partial derivatives with respect to ρ, l and D, we can obtain equations 3.7 and 3.8.

$$dR = \frac{4l}{\pi D^2} d\rho + \frac{4\rho}{\pi D^2} dl - \frac{8\rho l}{\pi D^3} dD \tag{3.7}$$

$$dR = \frac{4l}{\pi D^2} d\rho + \frac{4\rho}{\pi D^2} dl - \frac{8\rho l}{\pi D^3} dD \tag{3.8}$$

Gauge factor of metal foil strain gauges are shown by equations 3.9 and 3.10 in which first term is fractional change in resistivity and third term is the Poisson's ratio.

$$g = \frac{\frac{dR}{R}}{\frac{dl}{l}} = \frac{\frac{d\rho}{\rho}}{\frac{dl}{l}} + 1 - 2\frac{\frac{dD}{D}}{\frac{dl}{l}} \tag{3.9}$$

$$g = \frac{\frac{d\rho}{\rho}}{\frac{dl}{l}} + 1 + 2\vartheta \tag{3.10}$$

Nevertheless, sensitivity of metal foil strain gauges is nearly same as mercury strain sensor ($g \cong 2 - 4.5$). Fractional change in resistance due to force can be derived by equations 3.11 and 3.12. In these equations, F, σ and E are applied force, normal stress and Young's modulus of material.

$$F = \sigma E = \frac{EAdl}{l} = \frac{EAdR}{gR} \tag{3.11}$$

So, for high force sensitivity, small cross section area, small Young's modulus and high gauge factor are desired (equation 3.12). Elastic limit of most of materials is 1% that limits operation range of strain gauge.[67]

$$\frac{dR}{R} = \frac{Fg}{EA} \qquad 3.12$$

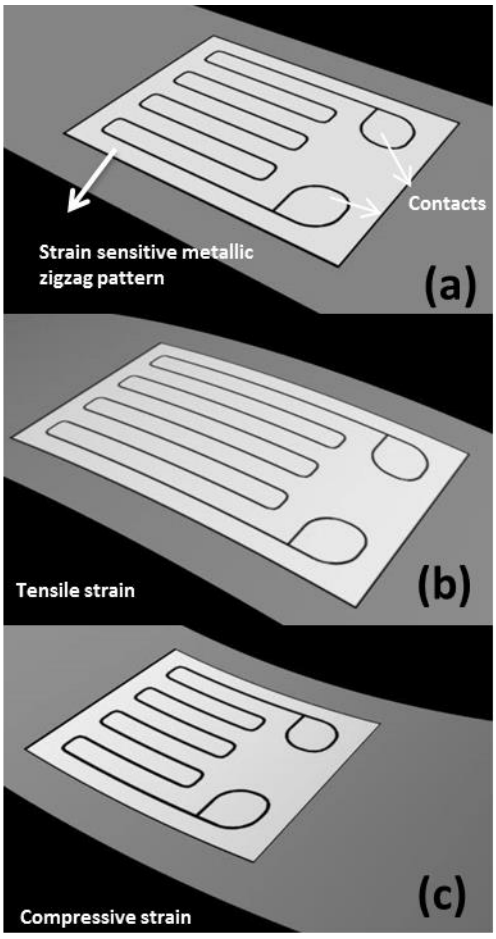

Figure 3-2 Metal foil strain gauge under (a) no strain(no change in the resistance) (b) tensile strain (zigzag pattern becomes longer and thinner resulting in increase of

resistance) (c) compressive strain (zigzag pattern becomes shorter and thicker resulting in decrease of resistance).

3.1.3 Semiconductor strain gauges

Another type of strain gauges is semiconductor strain gauge. Generally, p-doped silicon thin film is used because of high piezoresistive property. When strain is applied, band structure, electron effective mass, and mobility are changed. Semiconductor strain gauge is more sensitive than metal foil strain gauge. Gauge factor of semiconductor strain sensor is generally between 70 and 200. However, this type of strain gauges requires temperature compensation and has limited operation range. In order to avoid temperature, two sensors are placed so that one of its measure strain and another temperature effect[67].

3.1.4 Wheatstone bridge

Wheatstone bridge circuit is commonly used in strain gauges to sense the resistance change (Figure 3-3). In this circuit, identical resistors are used one of which is strain sensor's resistance. When there is no resistance $V_{out} = 0$, any change in strain gauge resistance can then be measured by V_{out} (equation 3.13).

$$V_{out} = V_{BA} = V_{in}\left(\frac{R_1}{R_1 + R_2} - \frac{R_3}{R_3 + R_4}\right) \qquad 3.13$$

So, under small resistance changes and identical resistors, we can approximate to equation 3.14 which is linear to strain.

$$V_{out} = \frac{V_{in}\Delta R}{4R} = \frac{V_{in}}{4} g\varepsilon \qquad 3.14$$

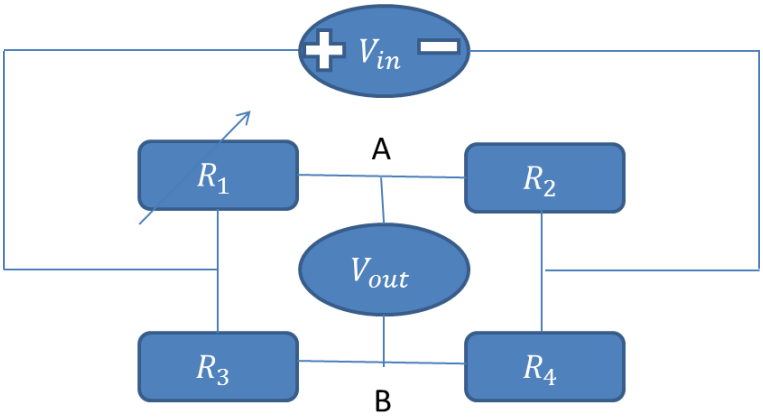

Figure 3-3 Wheatstone bridge circuit

3.1.5 Basic requirements of ideal strain gauge

Calibration constant of strain gauge should be very stable and does not depend on temperature and vary with time. Strain gauges require operation range between 0.001% and 1%. Working frequency range of the strain gauge should vary from DC to few kHz, which is generally limited by stray capacitance. In order to sense local strain at point, strain sensors with small gauge length are required. Linear response of strain gauges is preferable [67]. Also, strain gauge should be useful for other sensing elements such as pressure sensors.

3.2 Nanoparticle strain gauge

3.2.1 Conduction properties of Au-NP films

Recently, researchers demonstrate nanoparticle strain gauges that can present very high sensitivities [29]. These strain sensors are based on fundamentally different sensing mechanisms than conventional strain gauge. Working principle of nanoparticle strain gauge is based on quantum tunneling effect; therefore, it is possible to obtain highly sensitive strain gauges [29]. It is important to mention early studies of Au-NP film conductivity that lead to the progress of such applications. In the literature, the conduction behavior between chemically synthesized nanoparticles has been intensively studied [27, 28, 68, 69]. Schematic presentation of Au-NP film is shown in the Figure 3-4, where electrons are hopping between Au-NPs.

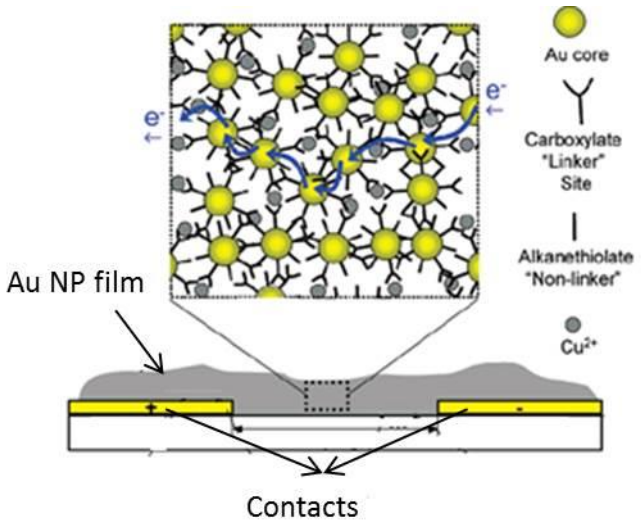

Figure 3-4 Shematic representation of electron hopping conductivity in Au-NP film. Adopted from Zamborini *et al.* (2002) [69]

The conduction of n-alkanethiol-stabilized Au-NP films has exponential decay dependence to the length of ligands' alkane chain (Figure 3-5).

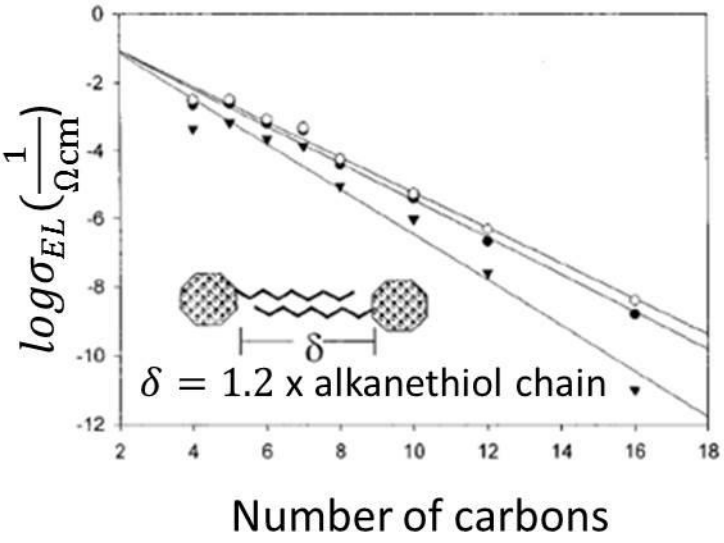

Figure 3-5 Exponential conductivity dependence on alkanethiol chain length. Adopted from Wuelfing *et al.* (2000)[28]

This effect is attributed to quantum tunneling effect [28, 69]. Conductivity of films was given by equation 3.15:

$$\sigma_{electronic}(n,T) = \sigma_0 e^{-d\beta - \frac{E_A}{RT}} \qquad 3.15$$

where d, β, E_A and R are distance between nanoparticle, which is equal to alkanethiolate chain length; the corresponding electronic coupling term, tunneling decay constant; the activation energy of conductivity; and the universal gas constant, respectively [27]. Tunneling decay constant is found to be between $8-12\,nm^{-1}$ for alkane chain and for saturated hydrocarbons is $\sim 10\,nm^{-1}$ [28, 70]. First exponential term, $e^{-d\beta}$, is because of tunneling effect; whereas, second exponential term, $e^{-\frac{E_A}{RT}}$, is

due to thermally activated conductance [70]. Thermally activated conduction mechanism is when electron is located in linker molecule between nanoparticles then; it can be delocalized in the molecule or diffuse by hopping between two nanoparticles [70].

3.2.2 Quantum tunneling effect

Quantum tunneling effect is highly depended on barrier width, which is distance between nanoparticles in the case of nanoparticle strain gauges, and height that depends on highest occupied molecular orbital (HOMO) and lowest unoccupied molecular orbital (LUMO) gap for molecules. If two same metal segments are very close to each other (<1nm) electrons will tunnel from one metal to another because of wave nature of electron. In this condition, there will be no net current because tunneling from both sides will cancel out each other. However, if one applies voltage difference between these segments, there will be net current due to energy difference between electrons in each segment.

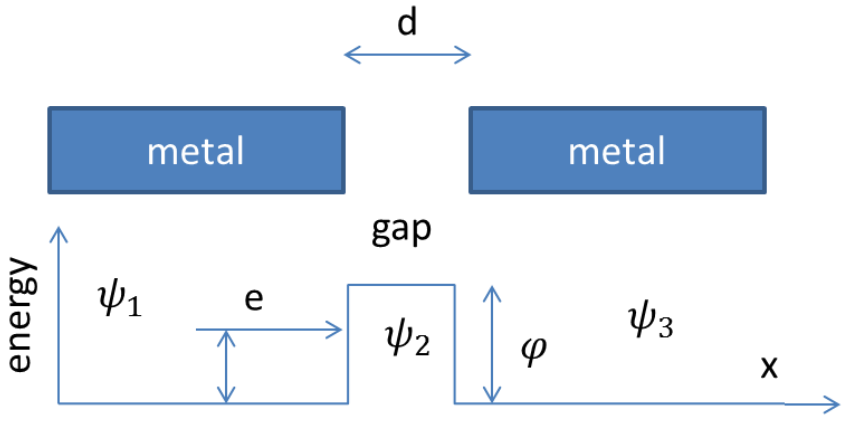

Figure 3-6 Schematic demonstration of quantum tunneling effect between two metal segments

$$-\frac{\hbar^2}{2m}\frac{\partial^2\psi}{\partial x^2} + U(x)\psi = E\psi \qquad 3.16$$

Amount of current can be calculated by solving time independent Schrödinger's equation (equation 3.16) for wave propagating through a potential barrier as shown in the Figure 3-6. In this equation, $U(x)$ is a potential barrier, which is $\sim\varphi$ for low energy electrons between two metals and zero outside the gap, where m is mass of electron; $\hbar$ is reduced Planck's constant; E is energy of electron; φ is work function of material. Transmission coefficient can be approximately shown by equation 3.17 for low electron energies where d is the distance between two metal segments.

$$T \cong \left(\frac{4k\alpha}{k^2+\alpha^2}\right)^2 \boldsymbol{e^{-2\alpha d}} \qquad 3.17$$

k and α are main parameters which determine strength of transmission probability given by the equations 3.18 and 3.19.

$$k^2 = \frac{2mE}{\hbar^2} \qquad 3.18$$

Particularly, α is important because it is on the exponential part of the equation 3.19.

$$\alpha^2 = \frac{2m(\varphi - E)}{\hbar^2} \qquad 3.19$$

Transmission coefficient is highly depended on width of tunneling barrier (equation 3.17). Because transmission coefficient is amplitude of the transmitted wave, the amount of transmitted electrons is proportional to T^2; so, tunneling current can be represented by equation 3.20 where β is the tunneling decay constant.

$$I = I_0 e^{-\beta d} \tag{3.20}$$

To illustrate, 0.1 nm displacement between to contacts which are very close to each other (gap<1nm) change in current is about 10 times. Work function of Au is ~5.4 eV, so tunneling decay constant can be found as $\sim 20\ nm^{-1}$ (equation 3.21).

$$\beta = 2\alpha = 2\sqrt{\frac{2m(\varphi - E)}{\hbar^2}} \approx 2\sqrt{\frac{2m\varphi}{\hbar^2}} \tag{3.21}$$

Fractional change in current can be found by using equation 3.22. This result is very exciting because 0.1 nm nearly same hydrogen atom size.

$$\frac{I_f}{I_{in}} = e^{-\beta(d_f - d_i)} = e^{20*0.1} = 10 \tag{3.22}$$

Because of this high sensitivity, tunneling effect is used in Scanning Tunneling Microscope (STM) which has ultimate resolution that can image individual atoms.

3.2.3 Au-NP strain gauge

The use of Au-NP in strain sensing has previously been reported in literature. J. Herrmann *et al*. demonstrated the high capability of Au-NP films to sense small linear strains [29]. These Au-NP films strain gauges were shown to be nearly two orders of magnitude sensitive than the conventional strain gauges.

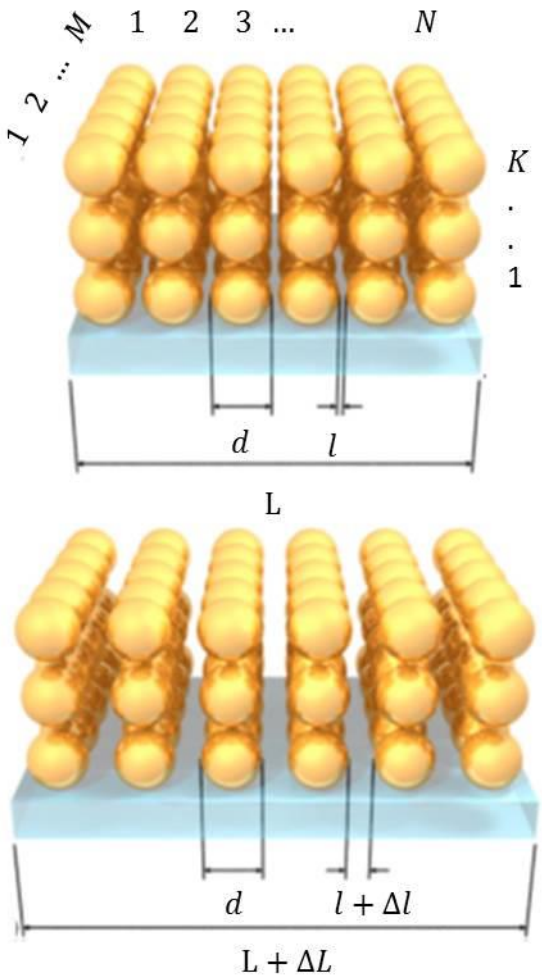

Figure 3-7 Schematic representation of Au-NP strain gauge. Adopted from Herrmann *et al.* (2007) [29]

In this section, Herrmann's simplified relation between strain and resistance change of nanoparticle films is derived [29]. In his study, resistance of Au-NP film will be $R_t = \frac{N}{MK}R$, where R is the resistance between two particles equals to $R = R_o e^{-\beta l}$; N,M and K are number of nanoparticles in different directions as shown in the Figure 3-7. Fractional change in resistance can be described by equation.

$$\frac{\Delta R}{R} = e^{\beta \Delta l} - 1 \qquad 3.23$$

Strain is proportional to change in distance between nanoparticles and inversely proportional to sum of the diameter and initial distance between nanoparticles, where we can only take in account diameter of nanoparticle if it's much larger than the distance between nanoparticles. Gauge length is shown by equation 3.24 where d is diameter of nanoparticle; l is gap between nanoparticles; N is number of nanoparticles.

$$L = N(d + l) \tag{3.24}$$

Change in length will cause only change in the nanoparticle separation; so, change in length can be shown by equation 3.25, where Δl is change in nanoparticle separation.

$$\Delta L = N\Delta l \tag{3.25}$$

Then, corresponding strain can be calculated by equation 3.26.

$$\varepsilon = \frac{\Delta L}{L} = \frac{\Delta l}{d + l} \tag{3.26}$$

Finally, fractional change in resistance can be derived where it has an exponential dependence to strain which is shown in the equation 3.27.

$$\frac{\Delta R}{R} = e^{g\varepsilon} - 1 \tag{3.27}$$

Gauge factor is proportional to tunneling decay constant and sum of the nanoparticle diameter and gap between nanoparticles. In the equation 3.27, we can see that gauge factor can be increased by both increasing tunneling decay constant and diameter of nanoparticle. Previous one is generally not easy to change as most of the saturated hydrocarbons which are used as ligands have nearly similar work functions [28, 70].

$$g = \beta(d + l) \qquad 3.28$$

If we have aggregates of nanoparticles, we can modify gauge factor formula, where d will average aggregate diameter, therefore, aggregation of nanoparticle can also play important role in sensitivity of Au-NP strain gauge [29].

Vossmeyer *et al.* (2008) demonstrated lower sensitivity - compared with Herrmann *et al*. (2007) results' - Au-NP strain sensors fabricated on flexible substrates by depositing 12-dodecylamine-stabilized Au-NPs via layer by layer self-assembly on oxidized flexible polyethylene. This technique provides high adhesion of Au-NPs on the substrate because of linker compound,1,9-nonanedithiol, which also increases the mechanical robustness of sensors.[30]

L. Ressier and coworkers (2011) developed stop-and-go convective self-assembly method to fabricate few micrometer wires based on Au-NPs, where separation of these Au-NP wires can be easily tuned [71]. These miniature strain gauges can be used for high sensitivity strain mapping. The monolayer wires of Au-NPs have higher strain sensitivity- gauge factor of 132- than multilayer wires[72]. They have also shown that gauge factor of Au-NP strain gauge is increasing while Au-NP diameter is increased. However, high sensitivity nanoparticle strain gauges, which are based on large nanoparticles, show significant hysteresis response when alternating strain is applied. [73].

Presence of chemical stabilizers on Au-NP surfaces potentially degrades the conductance and strain sensitivity according to equation 3.28. Films based on metal nanoparticles having clean surfaces were predicted to have improved gauge factors. Also, aggregates of nanoparticles can increase sensitivity [29].

Recently, Tanner *at el.* (2011) demonstrated that Pt nanoparticle coatings obtained by sputtering in vacuum present high gauge factors (700); however, the results were shown for very short strain range (0 to $60x10^{-6}$ strain) [74]. Tanner *et al.* (2011) have also shown that by increasing surface coverage resistance is increased because distance between nanoparticles decreases. Nanoparticle density in the films affects the sensitivity of Pt nanoparticle – radius of nanoparticles 4-5nm - strain gauge. In the films with surface coverage less than 50% of Pt nanoparticles, thermally assisted conduction is dominated; while for the films with the surface coverage more than 50%, conduction shows metallic behaviour. Highest sensitivity was achieved by 48% surface coverage, because of large effective radius as a result of clustering of nanoparticles (Figure 3-8).[75]

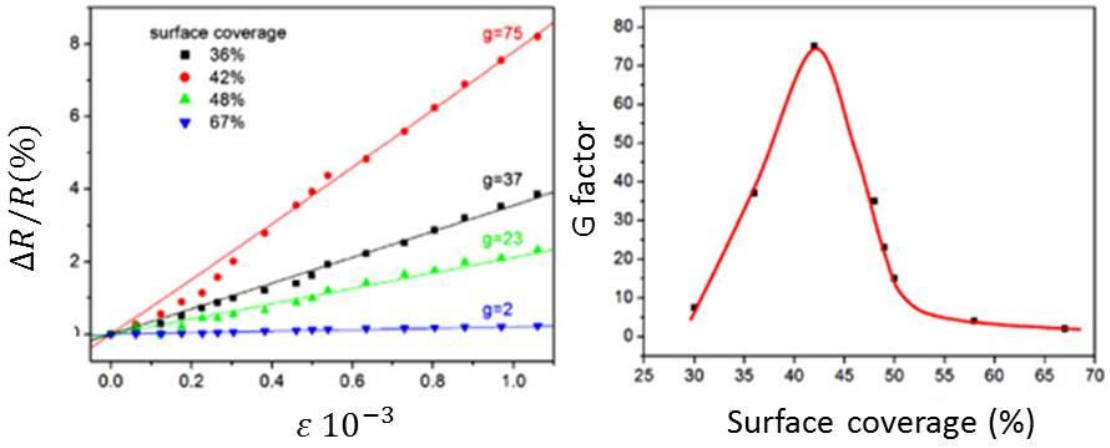

Figure 3-8 Surface coverage effect on sensitivity of Pt nanoparticle strain gauge where a) fractional change in resistance vs. strain and b) corresponding gauge factor for different surface coverage. Adopted from Tanner *et al.* (2012) [75].

Chapter 4

Laser synthesized Au-NP strain gauge

Some part of this chapter is published in *Sensors and Actuators A: Physical* as "Laser synthesized gold nanoparticles for high sensitive strain gauges".

4.1 Strain sensor fabrication

Deposition of Au-NPs on the surface plays an important role for strain sensor performance. First of all, the effect of localization of Au-NPs on the different insulating surfaces has been carried out. Au-NPs solution was dropped on the glass and silicon substrate; however, uniform thin film could not be successfully obtained due to hydrophilic nature of these surfaces. Thin films on glass and silicon were randomly distributed and mostly forming film at the edge of the droplet contact area. In the Figure 4-1(a), the glass surface is coated by Au-NPs at different concentrations which results in different coating formation. In Figure 4-1 (b), silicon nitride (Si_3N_4) surface with the initially fabricated Au contacts were deposited by Au-NPs. Although Si_3N_4 is hydrophobic, Au contacts are not; therefore, it was not possible to uniformly deposit Au-NPs.

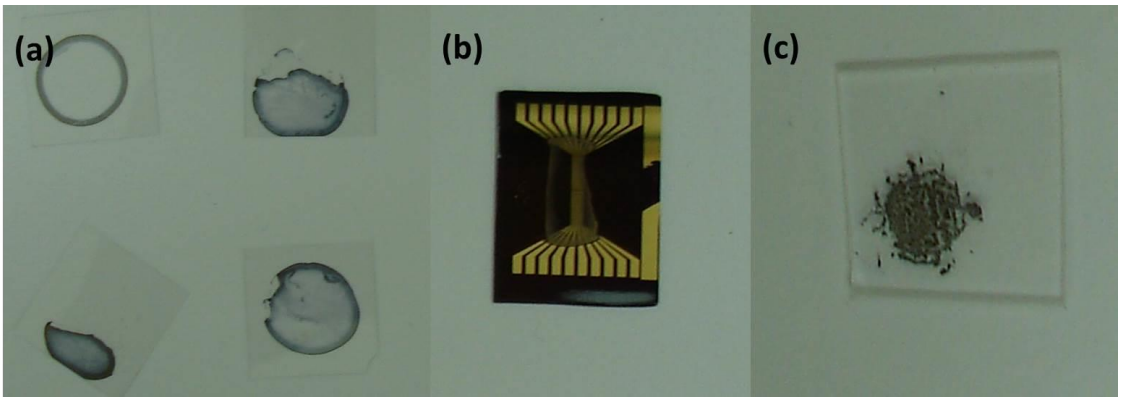

Figure 4-1 Au-NPs coating on different surfaces: (a) on glass at different concentrations; (b) on silicon nitride surface; (c) on PDMS at very high concentration.

On the other hand, polydimethylsiloxane (PDMS) substrate present low surface energy and hydrophobicity; thus, high contact angle. The high contact angle and low surface energy enables to uniformly precipitate particles and highly concentrate them on the surface. After droplet was completely dried, a dark blue spot was formed on the surface of PDMS. The color of the spot due to surface plasmon effect demonstrates that the Au-NPs are aggregated during drying. Au-NPs thin films obtained on PDMS were uniformly distributed (Figure 4-2(a)). Contacts were obtained using a shadow mask and a 350 µm gap was formed by coating 80 nm Pt film using sputtering (PECS Gatan 682) (Figure 4-2 (b)). It is also worth to note that at very high concentrations, Au-NPs solution on the PDMS, nanoparticles form large particles which can be seen by naked eye (Figure 4-1 (c)).

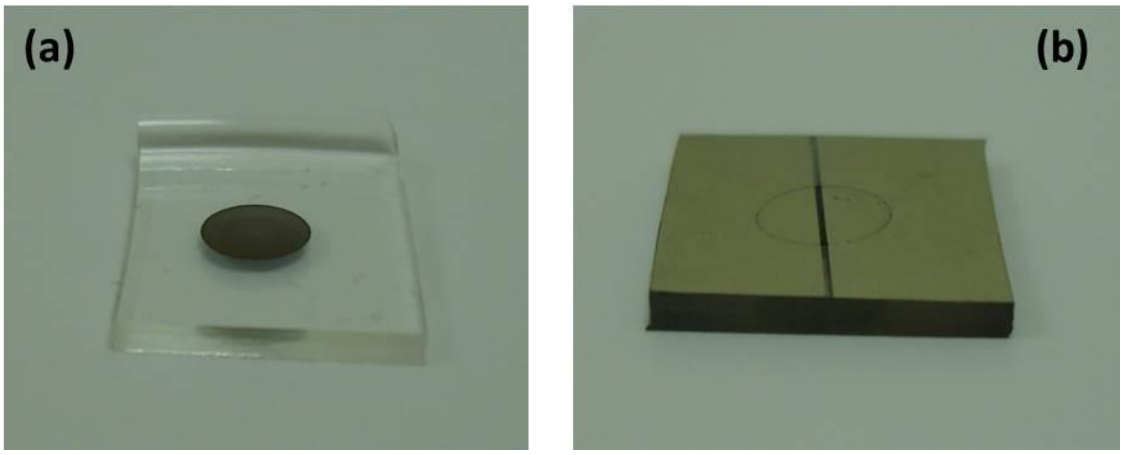

Figure 4-2 Au-NPs film on PDMS substrate. (a) Au-NPs film after droplet was dried. (b) After platinum contacts were deposited by PECS.

4.1.1 SEM images of Au-NP film

Scanning electron microscope (SEM) is a type of microscope that uses focused electron beam to produce images. Interaction of material with electron beam produces back-scattered electrons, secondary electrons, characteristic X-rays and light (cathodoluminescence). Secondary electrons are produced when high energy electrons, which are sent, interact with electrons in valence band. Secondary electrons are then ejected from the atoms and some of them have enough energy to escape from the surface. Then, these electrons can be used to image target surface. Fraction of ejected – number of sent electrons divided by number of secondary electrons obtained –electrons depend on the atomic number of the material which increases as atomic number increases. For example, for Au and carbon it is equal to 2 and 0.5 while for most of other element it is ~ 0.1. Because secondary electrons have low energies, there is certain threshold, namely the maximum escape depth, from which secondary electrons can be escaped. Typically, for metals and insulators it is 5 and 50 nm. Actually, most of the secondary electrons could not escape thickness between 2-5nm. Generally, SEM

specimen should be conductive and electrically grounded in order to avoid electrostatic charging of sample. Therefore, insulator specimens should be coated with metallic surfaces for avoiding charging of specimen. Coating such samples few nm with Au, Pt, Au/Pd will also increase number of secondary electrons due to relatively high atomic number of these elements.

SEM (FEI Nova NanoSEM 600) was used to further investigate the localization of Au-NPs on the PDMS substrate. In the SEM image, aggregated clusters can be seen, through which conduction takes place (Figure 4-3).

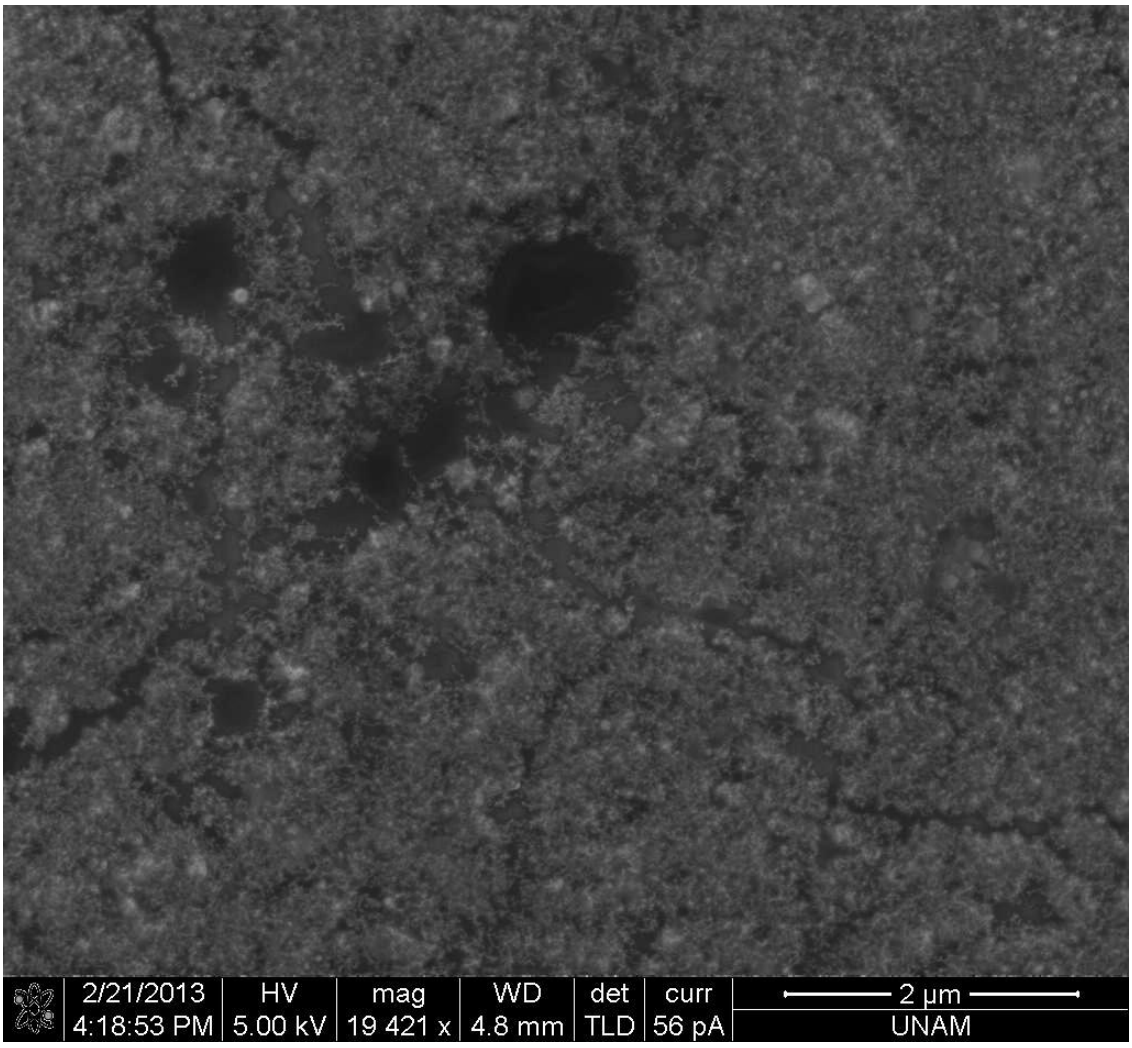

Figure 4-3 SEM image of Au-NPs thin film on PDMS substrate

4.1.2 Mechanical characterizations

Au-NPs based strain sensor was characterized by applying linear strain and observing change in resistance as shown in the Figure 4-4. Firstly, linear translation stage used to apply strain on the Au-NPs film. Pt contacts were first attached to two glass lamellas with silver paints. Then, glass lamellas were stuck to linear stage by epoxy. The gap between two lamellas was initially about 4.5 mm and applied strain was swept from 0 to 0.025 mm. Semiconductor Parameter Analyzer Keithley 4200-SCS was used to measure current output from Au-NPs film at 1V bias. Secondly, self-made strain measurement setup was employed to measure alternating strain response of the Au-NPs thin film strain sensor. 100 V piezoelectric actuator (Thorlabs AE0203D08F), 3-axis piezocontroller (Thorlabs MDT693A), current noise preamplifier (Stanford Research systems SR-570), function generator (Stanford Research Systems DS345) and oscilloscope (Tektronix TDS1012B) were used. In this setup, we have stuck Au-NPs strain gauges as in a waythat one side to movable linear stage and other part to fixed to the pedestal post where gap was about 1.3-1.4 mm. Piezoelectric actuator was placed inside movable linear stage; thus, it generates alternating strain with the square function of frequency 1 Hz and peak-to-peak amplitude ~ 9.1 μm. Dynamic measurements were performed by current noise preamplifier which is used to obtain current from Au-NPs strain gauge at 0.25 V bias; sensitivity was set to 5 nA ; and 3 Hz low pass filter was used.

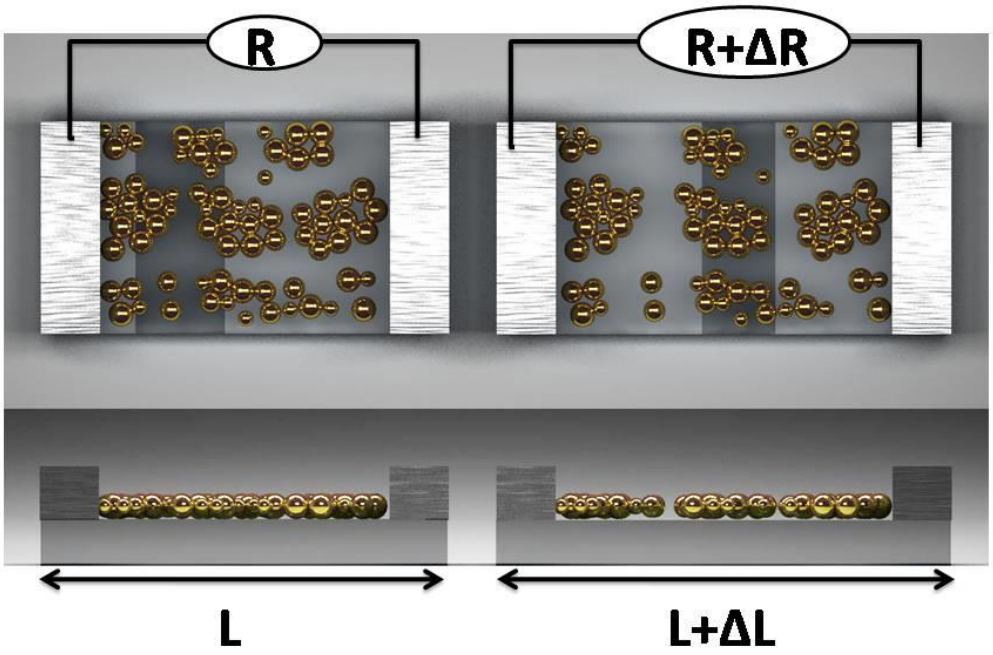

Figure 4-4 Schematic demonstration of Au-NPs strain gauge. Pt contacts are at the edges of sensor and Au-NPs are shown as yellow balls. Note that, dimensions are not to scale. In the left side, Au-NP film is in the initial state where there is no strain and resistance of film is R. In the right side, strain is applied to Au-NP film that increases distances between nanoparticles and aggregated clusters resulting in resistance increase of ΔR.

The concentration of the nanoparticles on the substrate strongly affects the conductivity and strain sensitivity of the Au-NP film. The concentration of Au in the Au-NPs in water obtained by ~10 min laser ablation was approximately $1.08\,mM$. Au mass in Au-NP colloidal solution was calculated by weighing the Au block before and after the ablation process. Then, the molarity value of Au in Au-NP solution was calculated in terms of mM. This colloidal solution was diluted several times to obtain solutions with different concentrations. $300\,\mu l$ of diluted solutions were applied to PDMS substrates and dried at ambient conditions to form spots with typical diameter of

5 mm. Films prepared with $> 0.9\,mM$ colloidal solutions were very conductive and did not respond to strain; while, films prepared with $< 0.72\,mM$ solutions were highly resistive (resistance $> 200\,M\Omega$) and sensitive to strain. It was observed that films that have higher resistance were more sensitive to strain. Optimal concentration for Au-NPs strain gauges is found to be about $\sim 0.81\,mM$ that yields high sensitivity and measurable resistance. Laser-synthesized nanoparticle solutions tended to aggregate due to absence of chemical stabilizers resulting in different film formation after several days.

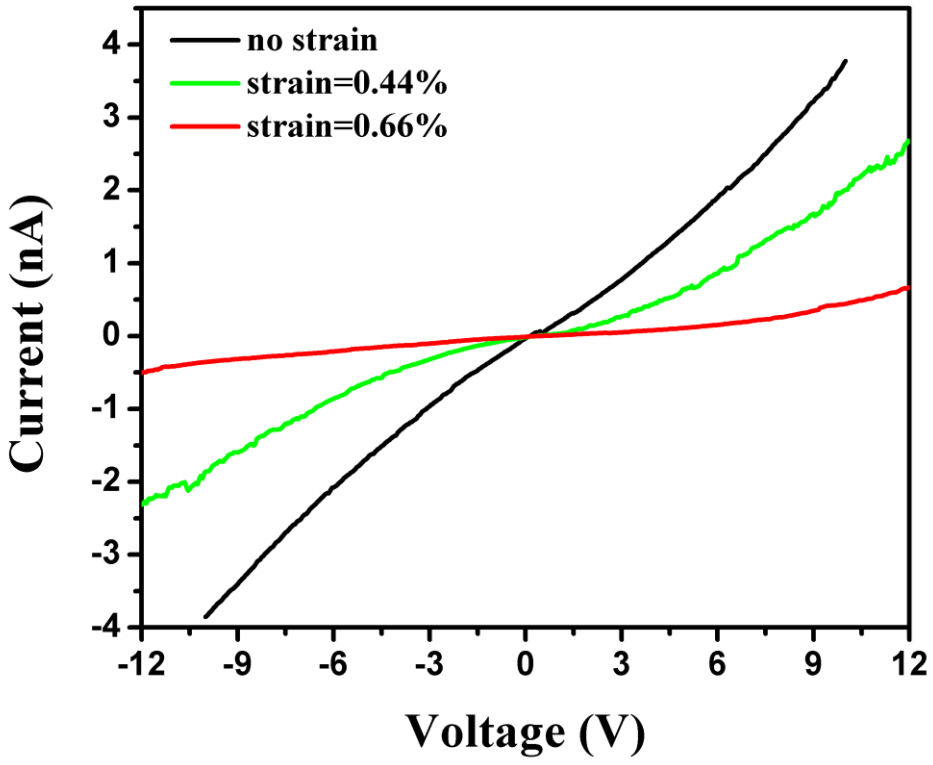

Figure 4-5 I-V curve of Au-NP film under different strains.

Electrical current versus voltage (I-V) curves of Au-NP film under different strains is shown in the Figure 4-5. When there is no strain I-V curve is nearly linear;

however, after certain threshold strain I-V curve reveal non-linear behavior. Nonlinear behavior can appear from the fact that tunneling decay constant depends on energy of electron; thus, on applied bias. Initially, in Au-NP film there may be some pathways where Au-NPs are in touch, so contact can be treated as Ohmic contact. After some amount of strain is applied, number of contact pathways decreased or disappeared and tunneling starts to be more significant in conduction of Au-NP film. In these regime, I-V curve can behave in the nonlinearly for higher voltages since tunneling decay constant also slowly decreases while voltage is increasing (equation 4.1 and 3.21).

$$I = \frac{V}{R_0} e^{-\beta l} \qquad 4.1$$

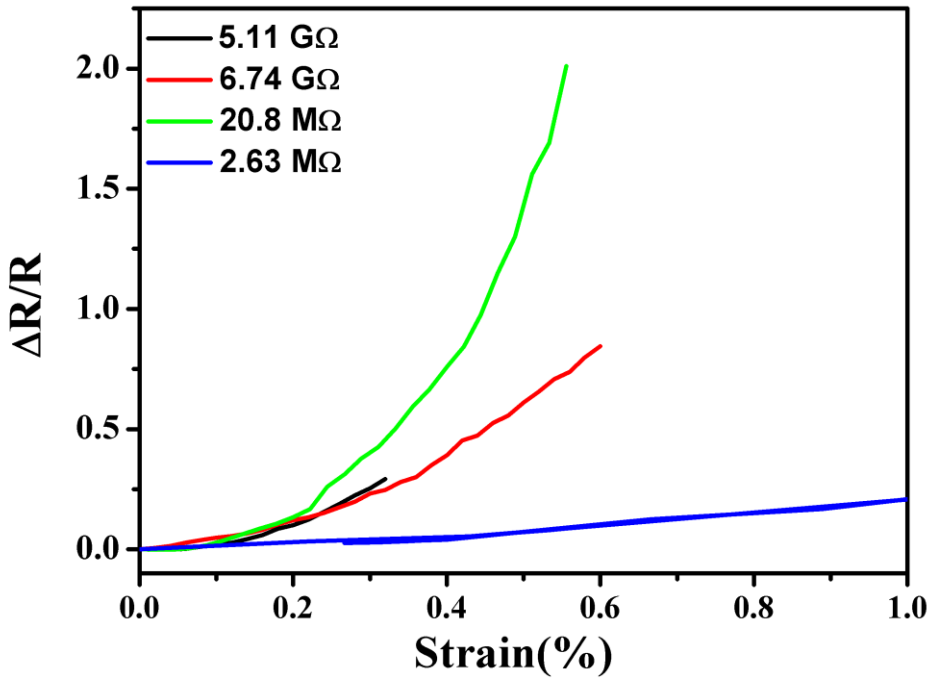

Figure 4-6 Resistance change of Au-NP film that have different initial resistances upon applying strain.

In the Figure 4-6, strain responses of Au-NP films with different initial resistances are studied. Resistance change of PDMS is not considered because resistance of PDMS is very large compared to that of Au-NP film. Interestingly, all Au-NP present nearly similar results at very small strain; however, for higher strain behavior of them will become different. Especially, Au-NP films with a high resistance reveal nearly same behavior to strain up to 0.2% (Figure 4-6). Generally, larger strains can be applied to Au-NP films that have low resistances while keeping the initial resistance reversible. On the other hand, the working range of Au-NP films that have high resistances is smaller compared to those which have lower resistances. In general, higher resistance show higher sensitivity but it is not always a case which is clearly seen in the Figure 4-6 . Highest sensitivity is observed for $20.8M\Omega$ Au-NP film. Nevertheless, different initial resistances can be obtained while fabricating the films. In addition, different sensitivities of these films are observed, which may not be similar to the Figure 4-6. These issues appear due to lack of control in fabrication technique. Also, control of separation between Au-NP, which is very important because of quantum tunneling effect, is not an easy without surface ligands.

Aggregated clusters might be also responsible for high sensitivity of Au-NP strain gauge since every cluster can be considered as a particle. In this scenario, aggregates remain unstrained while most of the deformation occurs between them. As a result, equation 3.28 can be modified in such way that d corresponds to average cluster diameter [29, 75].

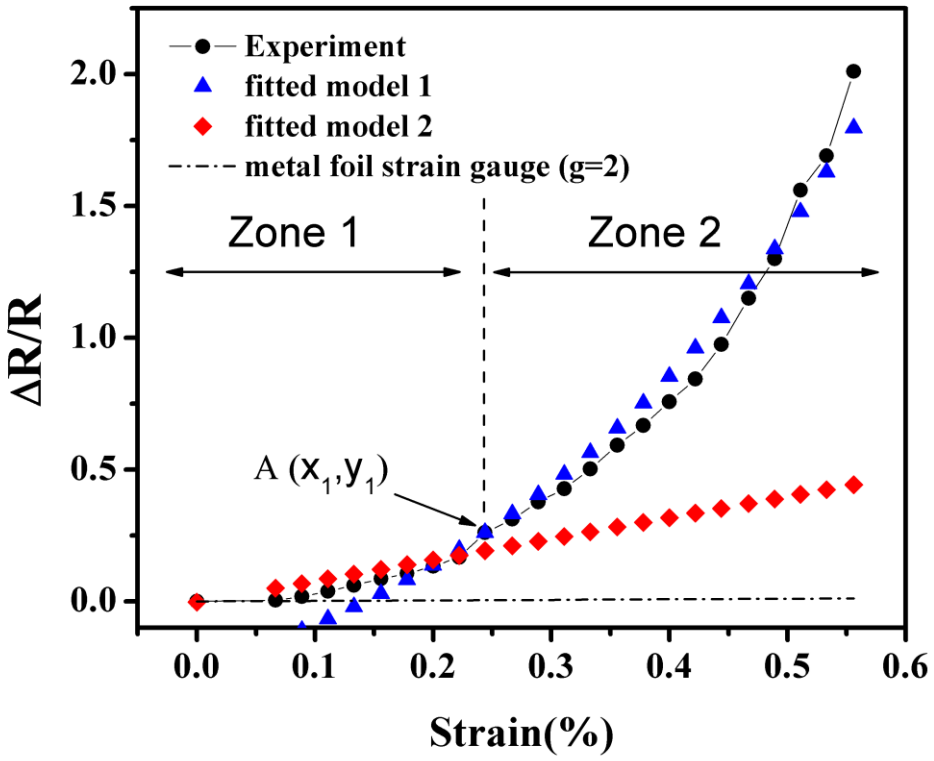

Figure 4-7 Resistance change response of Au-NP films while applying strain. Fit 1 and 2 are the corresponding linear and exponential functions. Also, metal foil strain gauge response is shown for comparison which have gauge factor of 2 (dashed-dotted line).

In the Figure 4-7, it is clearly seen that there is significant change in resistance of Au-NP film while the strain is being applied, which indicates higher sensitivity of Au-NP film than conventional metal foil strain gauges. Previously, the strain response of Au-NP strain sensor was explained by equation 3.27 ($\Delta R/R = exp(g\varepsilon) - 1$) where particles are initially separated from each other [29]. Strain response of the Au-NP film with initial resistance of 20.8 MΩ is shown in the Figure 4-7. It is observed that the Au-NP strain sensor response is linear under small strains (<0.22%). The gauge factor is obtained by fitting a function of the form:

$$\Delta R/R \approx g\varepsilon \quad (4.2)$$

which results in $g \cong 80.2$ under small strains (Figure 4-7, fit 1). Under higher strains (>0.22%) Au-NP film resistance is fitted with an exponential function of the form:

$$\frac{\Delta R}{R} - y_1 = \exp\big(g(\varepsilon - x_1)\big) - 1 \quad (4.3)$$

where $(x_1 y_1)$ is A point in the Figure 4-7 which results in an effective gauge factor of $g \cong 298$ (Figure 4-7, fit 2). Assuming that the tunneling undergoes in air, tunneling decay constant is $\sim 20\ nm^{-1}$ and average nanoparticle diameter is $\sim 13 - 15\ nm$; so, g can be approximated as a value of 300. [29]. Tunneling decay constant depends on the height of quantum barrier. Under low biases, $\beta \approx 2\sqrt{\frac{2m\varphi}{\hbar^2}}$ where m, φ and $\hbar$ are electron effective mass, work function and reduced Planck's constant, respectively.

One possible explanation for the presence of multiple regimes with distinct gauge factors is sought by considering the conduction mechanism in the Au-NP film. Initially, by proper choice of NP concentration, the films are prepared near the percolation threshold, with a large number of parallel conduction paths. Under the application of a small strain (zone 1 in the Figure 4-7), the number of paths contributing to conductance of the films diminishes, causing a linear increase in resistance described by equation 4.2. As the paths are broken at point A, conduction through the paths are dominated by tunneling (zone 2 in the Figure 4-7), which exhibits a larger resistance change. At the point $A(x_1, y_1)$, quantum tunneling starts to play

major role; as a result, equation 3.27 should be corrected to equation 4.3 so that exponential dependence begins from the point (x_1, y_1).

Modulation strain response of Au-NP strain gauge shows dynamic response of resistance (Figure 4-8). The initial resistance of this strain sensor used for this experiment was 11.11 MΩ. Gauge factor of Au-NP sensor used in this experiment is approximately 118. Strain response did not exhibit noticeable change after hours of operation. Also, reproducible responses can be taken even after weeks of initial preparation. For the frequencies larger than 1 Hz, sensitivity of the device starts to degrade because of low Young's modulus and viscoelastic property of PDMS.

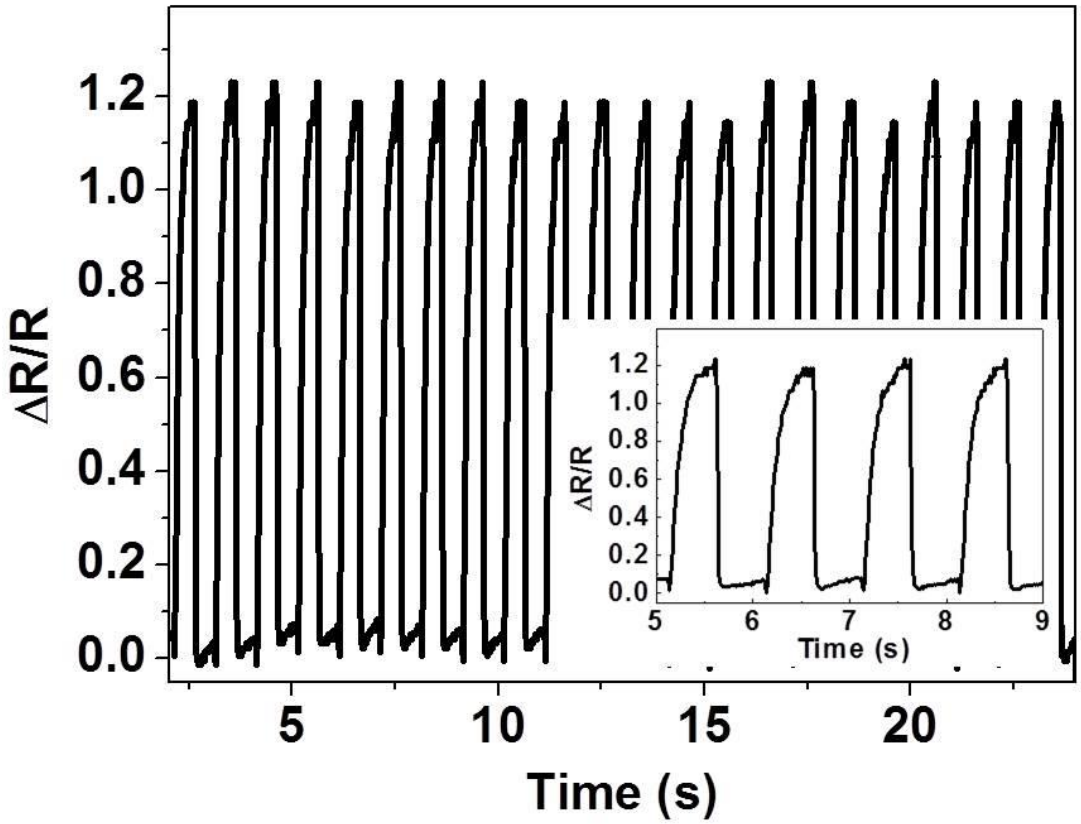

Figure 4-8 Alternating strain response of Au-NPs strain sensor (at 1Hz frequency). Resistance of Au-NP film is highly dependent on gaps between nanoparticles.

Statistical study is required in order to understand how Au-NP film resistance is dependent on gaps between Au-NPs. We made simulation where every gap is considered to be either series or parallel resistor (Figure 4-9). We perform numerical Monte-Carlo simulations to understand how the gaps between Au-NPs affect the resistance of the Au-NP strain sensor. Simmons's generalized formula for tunneling was used to obtain resistances of the samples[76]. Potential difference between the nanoparticles is assumed as the distance between nanoparticles times electric field ($V = El$) where electric field equals to applied bias divided by distance between to contacts ($E = V_{bias}/\ L$). Direct tunneling should be observed since potential difference between nanoparticles is small due to small ($< 1\ nm$) distances between nanoparticles. In the simulation, input was a random Gaussian distribution of the gaps (700*10 000 2D nanoparticles matrix, performed 1000 times) and output was number of samples vs. resistance of the samples. Figure 4-9 seems as a Gaussian distribution, which shows the number vs. resistances of samples. The gap between nanoparticles is 0.18 nm with standard deviation of 0.18 nm. In other words, the nanoparticles are very close to each other. This graph demonstrates that different substrates appear while drying same amount of Au-NPs on PDMS.

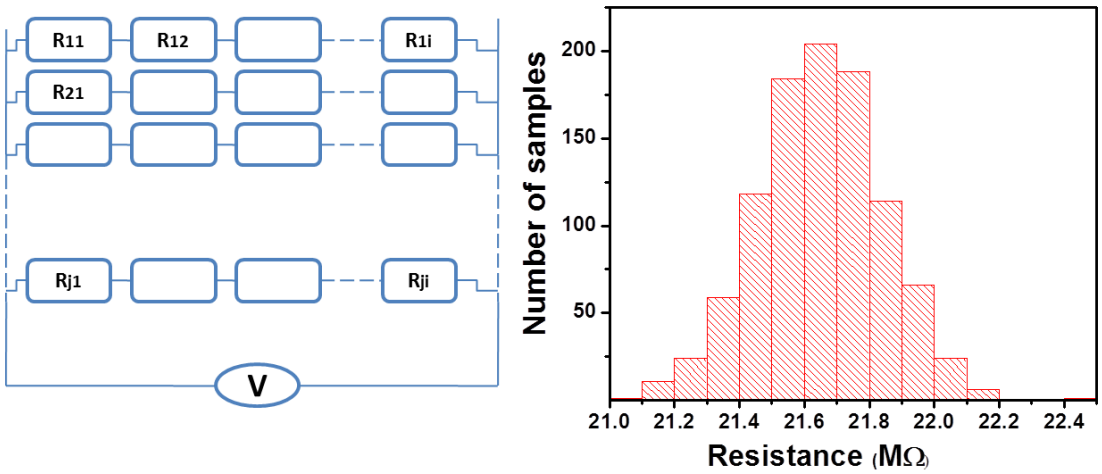

Figure 4-9 Simple circuit model of Au-NPs thin film and histogram of number of samples vs. resistance of the samples.

Chapter 5

Conclusion and outlook

In this thesis, we have demonstrated that laser generated Au-NP films on PDMS can be further used for highly sensitive strain gauge. In the first part, laser ablation method was studied. Heating of target surface was explained by two temperature model where electron and lattice temperature was considered. Electron and lattice temperature can be considered same for nanosecond laser ablation because electron phonon coupling is much faster than nanosecond light pulse. Material removal was also discussed which includes mainly thermal and plasma effects. In thermal process, normal vaporization and explosive boiling are considered as the main material removal mechanism in nanosecond laser ablation. Plasma, the ionized gas, also plays important role in laser ablation. Especially in liquids, plasma is more confined causing higher ablation yield than the ablation yield achieved in the vacuum. How combination of vaporized, melted and fragmented particles is involved in the nanoparticle growth was briefly discussed. Melted and fragmented particles appear mainly due to thermal effect; and vaporized atoms and molecules are mainly due to both thermal effect and plasma generation.

Also, brief information on strain gauge was given. Strain gauges are used to measure mechanical deformations. Au-NP strain gauges provide some advantages compared with conventional strain gauges. Mainly, these strain gauges have higher sensitivity, which is nearly two orders of magnitude higher than metallic strain gauges and comparable with semiconductor strain gauges. Also, size of this strain gauge can be very small. Therefore, it is possible to design miniature device for sensing strain in the single point.

Au-NPs were synthesized by laser ablation method in deionized water. TEM analysis shows that the size distribution is mainly in 5-25 nm range. Absorption spectra of colloidal solution have wide surface plasmon peak which confirms nanoparticle existence and wide size distribution. XPS studies are also done where low oxidation of nanoparticles is observed.

Simple drop-cast method was used to fabricate Au-NP film on different substrate surfaces. Relatively uniform films were obtained on hydrophobic surfaces such as PDMS. Distribution of nanoparticles on surface of PDMS was studied by SEM.

We have developed laser generated Au-NP strain gauge. Gauge factor of these films was found to be ~ 300 for strains higher than 0.22 %, which is the highest reported sensitivity for Au-NP strain sensors. High sensitivity properties of laser generated Au-NP strain sensors were attributed to clean surfaces, size and aggregated clusters of Au-NPs. High stability was also studied by self-made mechanical characterizations.

Several theoretical models were proposed in order to understand conduction properties of Au-NP films. Particularly, two mechanism were briefly explained,

conduction mechanism under low strains (<0.22%) and conduction mechanism for higher strains. Under low strains, resistance of film is decreased because the number of conduction paths is decreased. Under high strain, resistance change is determined by quantum tunneling effect which presents high strain sensitivity. Also, in order to understand how gap between nanoparticles affects total resistance of films, Monte-Carlo simulation was performed. In this numerical study, every gap was considered as series or parallel resistor. Gap distribution is found to have high impact on resistance of Au-NP film.

Laser synthesized Au-NP films present promising properties for sensing applications because these sensors are easily fabricated on PDMS substrate and have high strain sensitivity. PDMS, having low Young's modulus, is flexible substrate which can be advantageous for some applications such as low pressure sensing. It is easy to obtain uniform films on PDMS; however, this substrate has some drawbacks such as creep deformation, stress relaxation and high thermal coefficient. Depending on sensing applications, different substrates with hydrophobic surface, which allows uniform deposition of nanoparticles by drop-cast method, can be employed to develop Au-NP strain gauge. For example, substrates with high Young's modulus can increase operation frequency range of the device. Studies on deposition techniques may be required to improve adhesion of Au-NPs on the substrate which may improve mechanical robustness. Coating the Au-NP film with protection layer could also be required to reduce unwanted environmental effects such as variations in humidity. Nanoparticle size can be tuned to obtain desirable sensitivity and reproducibility. Smaller contacts can be employed for decreasing nominal resistance which in turn will

reduce noise associated with low current detection. In order to reduce variations in gauge factor, drop-casting on compressively strained substrate can be used. After relieving substrate it expands and all conducting path will be broken; as a result, only one regime (tunneling) will be responsible for resistance change in Au-NPs strain gauges. This will also make Au-NP film sensitive to compressive strain. For further studies; the reliability, the repeatability and the environmental effects such as gauge hysteresis, temperature dependence, long term aging, compression vs. tension deviation, sensitivity shift with number of cycles, etc. could be investigated for real-world applications of the Au-NP stain gauge.

Also, we observed that Au-NP film's resistance is sensitive to the humidity of the environment. We located Au-NP film in chamber where initial humidity was 25% (room humidity), then we pumped this chamber with a dry air (humidity changes to 3.7%). Afterwards, we opened the chamber in order to increase humidity again. In the Figure 5-1, resistance response to humidity change is shown, where "on" is when dry air is pumped, while "off" is when dry air is stopped pumping and chamber is opened. Resistance change in this experiment was about 10-15%. For better understanding, further investigations of Au-NP films could be studied for humidity sensor applications.

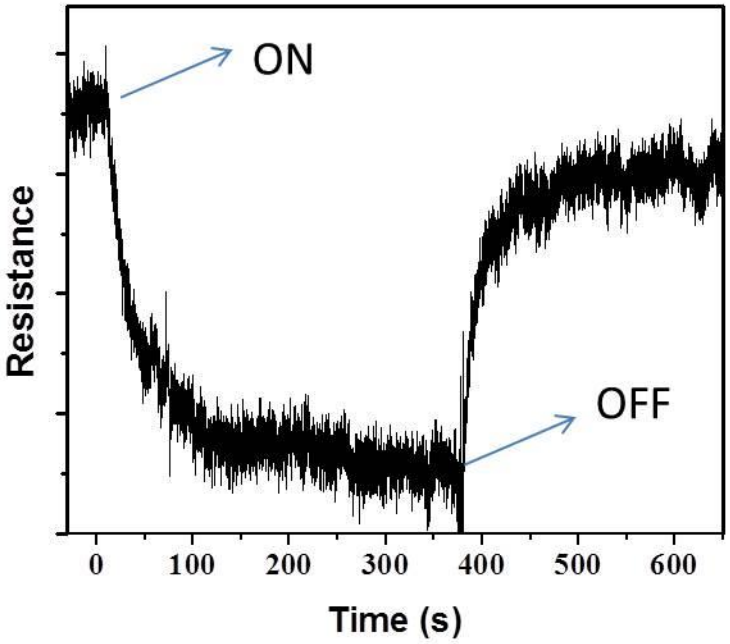

Figure 5-1 Au-NP resistance change due to humidity change. “ON” is when dry air is pumped, “OFF” is when dry air is stopped and container is opened.

Bibliography

[1] R. H. Brill, "The chemistry of the Lycurgus Cup," 1965.

[2] K. Novoselov, A. K. Geim, S. Morozov, D. Jiang, M. K. I. Grigorieva, S. Dubonos, and A. Firsov, "Two-dimensional gas of massless Dirac fermions in graphene," *nature,* vol. 438, pp. 197-200, 2005.

[3] R. Narayanan and M. A. El-Sayed, "Catalysis with Transition Metal Nanoparticles in Colloidal Solution: Nanoparticle Shape Dependence and Stability," *The Journal of Physical Chemistry B,* vol. 109, pp. 12663-12676, 2005/07/01 2005.

[4] L. Feng, S. Li, Y. Li, H. Li, L. Zhang, J. Zhai, Y. Song, B. Liu, L. Jiang, and D. Zhu, "Super-Hydrophobic Surfaces: From Natural to Artificial," *Advanced Materials,* vol. 14, pp. 1857-1860, 2002.

[5] T. Sun, L. Feng, X. Gao, and L. Jiang, "Bioinspired Surfaces with Special Wettability," *Accounts of Chemical Research,* vol. 38, pp. 644-652, 2005/08/01 2005.

[6] S. Chakraborty, R. Thomas, and S. Maity, "Melting of nanoparticles."

[7] W. K. Leutwyler, S. L. Bürgi, and H. Burgl, "Semiconductor clusters, nanocrystals, and quantum dots," *Science,* vol. 271, p. 933, 1996.

[8] S. Eustis and M. A. El-Sayed, "Why gold nanoparticles are more precious than pretty gold: Noble metal surface plasmon resonance and its enhancement of the radiative and nonradiative properties of nanocrystals of different shapes," *Chemical Society Reviews,* vol. 35, pp. 209-217, 2006.

[9] D. Schooss, A. Mews, A. Eychmüller, and H. Weller, "Quantum-dot quantum well CdS/HgS/CdS: Theory and experiment," *Physical Review B,* vol. 49, pp. 17072-17078, 1994.

[10] Y. Horikoshi, M. Kawashima, and H. Yamaguchi, "Low-temperature growth of GaAs and AlAs-GaAs quantum-well layers by modified molecular beam epitaxy," *Jpn. J. Appl. Phys,* vol. 25, p. L868, 1986.

[11] G. Konstantatos, I. Howard, A. Fischer, S. Hoogland, J. Clifford, E. Klem, L. Levina, and E. H. Sargent, "Ultrasensitive solution-cast quantum dot photodetectors," *nature,* vol. 442, pp. 180-183, 2006.

[12] J. Zhao, J. A. Bardecker, A. M. Munro, M. S. Liu, Y. Niu, I. K. Ding, J. Luo, B. Chen, A. K. Y. Jen, and D. S. Ginger, "Efficient CdSe/CdS Quantum Dot Light-Emitting Diodes Using a Thermally Polymerized Hole Transport Layer," *Nano Letters,* vol. 6, pp. 463-467, 2006/03/01 2006.

[13] A. N. Oraevsky, M. Scully, and V. L. Velichansky, "Quantum dot laser," *Quantum electronics,* vol. 28, p. 203, 1998.

[14] M. Radosavljevic, B. Chu-Kung, S. Corcoran, G. Dewey, M. K. Hudait, J. M. Fastenau, J. Kavalieros, W. K. Liu, D. Lubyshev, M. Metz, K. Millard, N. Mukherjee, W. Rachmady, U. Shah, and R. Chau, "Advanced high-K gate dielectric for high-performance short-channel $In_{0.7}Ga_{0.3}As$ quantum well field effect transistors on silicon substrate for low power logic applications," in *Electron Devices Meeting (IEDM), 2009 IEEE International*, 2009, pp. 1-4.

[15] R. H. Baughman, A. A. Zakhidov, and W. A. de Heer, "Carbon Nanotubes--the Route Toward Applications," *Science,* vol. 297, pp. 787-792, August 2, 2002 2002.

[16] A. Javey, J. Guo, Q. Wang, M. Lundstrom, and H. Dai, "Ballistic carbon nanotube field-effect transistors," *nature,* vol. 424, pp. 654-657, 2003.

[17] J. N. Coleman, U. Khan, W. J. Blau, and Y. K. Gun'ko, "Small but strong: A review of the mechanical properties of carbon nanotube–polymer composites," *Carbon,* vol. 44, pp. 1624-1652, 2006.

[18] A. H. Castro Neto, F. Guinea, N. M. R. Peres, K. S. Novoselov, and A. K. Geim, "The electronic properties of graphene," *Reviews of Modern Physics,* vol. 81, pp. 109-162, 2009.

[19] A. K. Geim and K. S. Novoselov, "The rise of graphene," *Nature Materials,* vol. 6, pp. 183-191, 2007.

[20] S. Lindsay, *Introduction to nanoscience*: Oxford University Press, 2009.

[21] V. Amendola and M. Meneghetti, "What controls the composition and the structure of nanomaterials generated by laser ablation in liquid solution?," *Physical Chemistry Chemical Physics,* vol. 15, pp. 3027-3046, 2013.

[22] C. Momma, B. N. Chichkov, S. Nolte, F. vonAlvensleben, A. Tunnermann, H. Welling, and B. Wellegehausen, "Short-pulse laser ablation of solid targets," *Optics Communications,* vol. 129, pp. 134-142, Aug 1 1996.

[23] M. Muniz-Miranda, C. Gellini, and E. Giorgetti, "Surface-Enhanced Raman Scattering from Copper Nanoparticles Obtained by Laser Ablation," *The Journal of Physical Chemistry C,* vol. 115, pp. 5021-5027, 2011/03/31 2011.

[24] A. Nath and A. Khare, "Size induced structural modifications in copper oxide nanoparticles synthesized via laser ablation in liquids," *Journal of Applied Physics,* vol. 110, pp. -, 2011.

[25] W. T. Nichols, T. Sasaki, and N. Koshizaki, "Laser ablation of a platinum target in water. I. Ablation mechanisms," *Journal of Applied Physics,* vol. 100, Dec 1 2006.

[26] P. Liu, Y. L. Cao, H. Cui, X. Y. Chen, and G. W. Yang, "Synthesis of GaN Nanocrystals through Phase Transition from Hexagonal to Cubic Structures upon Laser Ablation in Liquid," *Crystal Growth & Design,* vol. 8, pp. 559-563, 2008/02/01 2008.

[27] R. H. Terrill, T. A. Postlethwaite, C. H. Chen, C. D. Poon, A. Terzis, A. D. Chen, J. E. Hutchison, M. R. Clark, G. Wignall, J. D. Londono, R. Superfine, M. Falvo, C. S. Johnson, E. T. Samulski, and R. W. Murray, "Monolayers in three dimensions: NMR, SAXS, thermal, and electron hopping studies of alkanethiol stabilized gold clusters," *Journal of the American Chemical Society,* vol. 117, pp. 12537-12548, Dec 20 1995.

[28] W. P. Wuelfing, S. J. Green, J. J. Pietron, D. E. Cliffel, and R. W. Murray, "Electronic conductivity of solid-state, mixed-valent, monolayer-protected Au clusters," *Journal of the American Chemical Society,* vol. 122, pp. 11465-11472, Nov 22 2000.

[29] J. Herrmann, K. H. Muller, T. Reda, G. R. Baxter, B. Raguse, G. J. J. B. de Groot, R. Chai, M. Roberts, and L. Wieczorek, "Nanoparticle films as sensitive strain gauges," *Applied Physics Letters,* vol. 91, Oct 29 2007.

[30] T. Vossmeyer, C. Stolte, M. Ijeh, A. Kornowski, and H. Weller, "Networked gold-nanoparticle coatings on polyethylene: Charge transport and strain sensitivity," *Advanced Functional Materials,* vol. 18, pp. 1611-1616, Jun 11 2008.

[31] S. Nolte, C. Momma, H. Jacobs, A. Tunnermann, B. N. Chichkov, B. Wellegehausen, and H. Welling, "Ablation of metals by ultrashort laser pulses," *Journal of the Optical Society of America B-Optical Physics,* vol. 14, pp. 2716-2722, Oct 1997.

[32] S. Anisimov, "Vaporization of metal absorbing laser radiation," *Sov. Phys., JETP,* vol. 27, pp. 182-183, 1968.

[33] V. Batanov, F. Bunkin, A. Prokhorov, and V. Fedorov, "Evaporation of metallic targets caused by intense optical radiation," *Soviet Physics-JETP,* vol. 36, pp. 311-322, 1973.

[34] B. N. Chichkov, C. Momma, S. Nolte, F. Alvensleben, and A. Tünnermann, "Femtosecond, picosecond and nanosecond laser ablation of solids," *Applied Physics A,* vol. 63, pp. 109-115, 1996/08/01 1996.

[35] Kaganov, M. I., I. M. Lifshitz, and L. V. Tanatarov. "Relaxation between electrons and the crystalline lattice." Sov. Phys. JETP 4.2 (1957): 173.

[36] ANISIMOV, S. I. Kapeliov. Bl, and TL Perelman. Electron-Emission from Surface of Metals Induced by Ultrashort Laser Pulses, 1974, 776-781.

[37] C. Momma, S. Nolte, B. N. Chichkov, F. vonAlvensleben, and A. Tunnermann, "Precise laser ablation with ultrashort pulses," *Applied Surface Science,* vol. 109, pp. 15-19, Feb 1997.

[38] D. Perez and L. J. Lewis, "Molecular-dynamics study of ablation of solids under femtosecond laser pulses," *Physical Review B,* vol. 67, p. 184102, 2003.

[39] Y. Afanasyev, O. Krokhin, and G. Sklizkov, "7A5 - Evaporation and heating of a substance due to laser radiation," *Quantum Electronics, IEEE Journal of,* vol. 2, pp. 483-486, 1966.

[40] K. H. Leitz, B. Redlingshofer, Y. Reg, A. Otto, and M. Schmidt, "Metal Ablation with Short and Ultrashort Laser Pulses," *Lasers in Manufacturing 2011: Proceedings of the Sixth International Wlt Conference on Lasers in Manufacturing, Vol 12, Pt B,* vol. 12, pp. 230-238, 2011.

[41] A. Miotello and R. Kelly, "Laser-induced phase explosion: new physical problems when a condensed phase approaches the thermodynamic critical temperature," *Applied Physics a-Materials Science & Processing,* vol. 69, pp. S67-S73, Dec 1999.

[42] M. Martynyuk, "Vaporization and boiling of liquid metal in an exploding wire," *Soviet Physics Technical Physics,* vol. 19, p. 793, 1974.

[43] M. Martynyuk, "Critical constants of metals," *Russ. J. Phys. Chem.,* vol. 57, pp. 494-500, 1983.
[44] N. M. Bulgakova and A. V. Bulgakov, "Pulsed laser ablation of solids: transition from normal vaporization to phase explosion," *Applied Physics a-Materials Science & Processing,* vol. 73, pp. 199-208, Aug 2001.
[45] M. Hashida, H. Mishima, S. Tokita, and S. Sakabe, "Non-thermal ablation of expanded polytetrafluoroethylene with an intense femtosecond-pulse laser," *Optics Express,* vol. 17, pp. 13116-13121, 2009.
[46] T. Asahi, T. Sugiyama, and H. Masuhara, "Laser Fabrication and Spectroscopy of Organic Nanoparticles," *Accounts of Chemical Research,* vol. 41, pp. 1790-1798, Dec 2008.
[47] T. Sakka, S. Iwanaga, Y. H. Ogata, A. Matsunawa, and T. Takemoto, "Laser ablation at solid–liquid interfaces: An approach from optical emission spectra," *The Journal of Chemical Physics,* vol. 112, p. 8645, 2000.
[48] R. Fabbro, J. Fournier, P. Ballard, D. Devaux, and J. Virmont, "Physical study of laser-produced plasma in confined geometry," *Journal of Applied Physics,* vol. 68, pp. 775-784, 1990.
[49] Y. Sano, N. Mukai, K. Okazaki, and M. Obata, "Residual stress improvement in metal surface by underwater laser irradiation," *Nuclear Instruments & Methods in Physics Research Section B-Beam Interactions with Materials and Atoms,* vol. 121, pp. 432-436, Jan 1997.
[50] D. Perez, L. K. Beland, D. Deryng, L. J. Lewis, and M. Meunier, "Numerical study of the thermal ablation of wet solids by ultrashort laser pulses," *Physical Review B,* vol. 77, Jan 2008.
[51] T. Tsuji, D. H. Thang, Y. Okazaki, M. Nakanishi, Y. Tsuboi, and M. Tsuji, "Preparation of silver nanoparticles by laser ablation in polyvinylpyrrolidone solutions," *Applied Surface Science,* vol. 254, pp. 5224-5230, Jun 15 2008.
[52] A. De Giacomo, M. Dell'Aglio, O. De Pascale, and M. Capitelli, "From single pulse to double pulse ns-Laser Induced Breakdown Spectroscopy under water: Elemental analysis of aqueous solutions and submerged solid samples," *Spectrochimica Acta Part B-Atomic Spectroscopy,* vol. 62, pp. 721-738, Aug 2007.
[53] J. H. Yoo, S. H. Jeong, X. L. Mao, R. Greif, and R. E. Russo, "Evidence for phase-explosion and generation of large particles during high power nanosecond laser ablation of silicon," *Applied Physics Letters,* vol. 76, pp. 783-785, Feb 7 2000.
[54] L. V. Zhigilei, "Dynamics of the plume formation and parameters of the ejected clusters in short-pulse laser ablation," *Applied Physics a-Materials Science & Processing,* vol. 76, pp. 339-350, Mar 2003.
[55] V. Amendola and M. Meneghetti, "Laser ablation synthesis in solution and size manipulation of noble metal nanoparticles," *Physical Chemistry Chemical Physics,* vol. 11, pp. 3805-3821, 2009.
[56] W. T. Nichols, T. Sasaki, and N. Koshizaki, "Laser ablation of a platinum target in water. II. Ablation rate and nanoparticle size distributions," *Journal of Applied Physics,* vol. 100, Dec 1 2006.

[57] A. V. Kabashin and M. Meunier, "Synthesis of colloidal nanoparticles during femtosecond laser ablation of gold in water," *Journal of Applied Physics*, vol. 94, pp. 7941-7943, Dec 15 2003.

[58] F. Mafuné, J.-y. Kohno, Y. Takeda, T. Kondow, and H. Sawabe, "Formation and Size Control of Silver Nanoparticles by Laser Ablation in Aqueous Solution," *The Journal of Physical Chemistry B,* vol. 104, pp. 9111-9117, 2000/10/01 2000.

[59] T. Tsuji, Y. Tsuboi, N. Kitamura, and M. Tsuji, "Microsecond-resolved imaging of laser ablation at solid–liquid interface: investigation of formation process of nano-size metal colloids," *Applied Surface Science,* vol. 229, pp. 365-371, 2004.

[60] W. T. Nichols, T. Sasaki, and N. Koshizaki, "Laser ablation of a platinum target in water. III. Laser-induced reactions," *Journal of Applied Physics,* vol. 100, Dec 1 2006.

[61] T. Tsuji, K. Iryo, Y. Nishimura, and M. Tsuji, "Preparation of metal colloids by a laser ablation technique in solution: influence of laser wavelength on the ablation efficiency (II)," *Journal of Photochemistry and Photobiology a-Chemistry,* vol. 145, pp. 201-207, Dec 3 2001.

[62] T. Tsuji, K. Iryo, H. Ohta, and Y. Nishimura, "Preparation of metal colloids by a laser ablation technique in solution: Influence of laser wavelength on the efficiencies of colloid formation," *Japanese Journal of Applied Physics Part 2-Letters,* vol. 39, pp. L981-L983, Oct 1 2000.

[63] T. Tsuji, K. Iryo, N. Watanabe, and M. Tsuji, "Preparation of silver nanoparticles by laser ablation in solution: influence of laser wavelength on particle size," *Applied Surface Science,* vol. 202, pp. 80-85, Dec 15 2002.

[64] E. D. Palik, *Handbook of Optical Constants of Solids: Index* vol. 3: Access Online via Elsevier, 1998.

[65] A. Szytula, D. Fus, B. Penc, and A. Jezierski, "Electronic structure of RTX (R=Pr, Nd; T=Cu, Ag, Au; X=Ge, Sn) compounds," *Journal of Alloys and Compounds,* vol. 317, pp. 340-346, Apr 12 2001.

[66] P. Marcus and M. E. Bussell, "Xps Study of the Passive Films Formed on Nitrogen-Implanted Austenitic Stainless-Steels," *Applied Surface Science,* vol. 59, pp. 7-21, May 1992.

[67] J. S. Wilson, *Sensor technology handbook*. Amsterdam ; Boston: Elsevier/Newnes, 2005.

[68] M. Brust, D. Bethell, C. J. Kiely, and D. J. Schiffrin, "Self-assembled gold nanoparticle thin films with nonmetallic optical and electronic properties," *Langmuir,* vol. 14, pp. 5425-5429, Sep 15 1998.

[69] F. P. Zamborini, M. C. Leopold, J. F. Hicks, P. J. Kulesza, M. A. Malik, and R. W. Murray, "Electron hopping conductivity and vapor sensing properties of flexible network polymer films of metal nanoparticles," *J Am Chem Soc,* vol. 124, pp. 8958-64, Jul 31 2002.

[70] D. M. Adams, L. Brus, C. E. D. Chidsey, S. Creager, C. Creutz, C. R. Kagan, P. V. Kamat, M. Lieberman, S. Lindsay, R. A. Marcus, R. M. Metzger, M. E. Michel-Beyerle, J. R. Miller, M. D. Newton, D. R. Rolison, O. Sankey, K. S.

Schanze, J. Yardley, and X. Y. Zhu, "Charge transfer on the nanoscale: Current status," *Journal of Physical Chemistry B,* vol. 107, pp. 6668-6697, Jul 17 2003.

[71] C. Farcau, N. M. Sangeetha, H. Moreira, B. Viallet, J. Grisolia, D. Ciuculescu-Pradines, and L. Ressier, "High-Sensitivity Strain Gauge Based on a Single Wire of Gold Nanoparticles Fabricated by Stop-and-Go Convective Self-Assembly," *Acs Nano,* vol. 5, pp. 7137-7143, Sep 2011.

[72] C. Farcau, H. Moreira, B. Viallet, J. Grisolia, D. Ciuculescu-Pradines, C. Amiens, and L. Ressier, "Monolayered Wires of Gold Colloidal Nanoparticles for High-Sensitivity Strain Sensing," *Journal of Physical Chemistry C,* vol. 115, pp. 14494-14499, Aug 4 2011.

[73] N. M. Sangeetha, N. Decorde, B. Viallet, G. Viau, and L. Ressler, "Nanoparticle-Based Strain Gauges Fabricated by Convective Self Assembly: Strain Sensitivity and Hysteresis with Respect to Nanoparticle Sizes," *Journal of Physical Chemistry C,* vol. 117, pp. 1935-1940, Jan 31 2013.

[74] J. L. Tanner, D. Mousadakos, P. Broutas, S. Chatzandroulis, Y. S. Raptis, and D. Tsoukalas, "Nanoparticle strain sensor," *Eurosensors Xxv,* vol. 25, 2011.

[75] J. L. Tanner, D. Mousadakos, K. Giannakopoulos, E. Skotadis, and D. Tsoukalas, "High strain sensitivity controlled by the surface density of platinum nanoparticles," *Nanotechnology,* vol. 23, Jul 20 2012.

[76] J. G. Simmons, "Generalized Formula for the Electric Tunnel Effect between Similar Electrodes Separated by a Thin Insulating Film," *Journal of Applied Physics,* vol. 34, pp. 1793-1803, 1963.